2023-12-18

Reliably quantifying asynchronisation between local representations of UTC

Bayat, Ashkan

UNIVERSITY OF CALGARY

Reliably quantifying asynchronisation between local representations of UTC

by

Ashkan Bayat

A THESIS
SUBMITTED TO THE FACULTY OF GRADUATE STUDIES
IN PARTIAL FULFILMENT OF THE REQUIREMENTS FOR THE
DEGREE OF MASTER OF SCIENCE

GRADUATE PROGRAM IN PHYSICS AND ASTRONOMY

CALGARY, ALBERTA
DECEMBER, 2023

Abstract

Asynchronisation is a major limiting factor for Coordinated Universal time (UTC) performance, and, by extension, other clock-network concepts, and our aim is to quantify asynchronisation reliably between different local representations of UTC, known as UTC(k) for k the site label. To this end, we devise a simple but faithful physical model and mathematical description for quantifying asynchronisation reliably between different UTC(k). Our UTC mathematical model comprises coupled Ornstein-Uhlenbeck (OU) processes, each representing UTC(k), which we discuss physically as a network of ballistic clocks network managed by a controller; for clarity we illustrate this network in the context of the sport of curling with the ballistic clocks pictured as curling stones. From our closed-form solution, we establish how to quantify asynchronisation reliably. Furthermore, we extend our ballistic-clock model to accommodate quantum effects, namely squeezing and entanglement, and analyse potential quantum advantage. Our approach to reliably quantifying asynchronisation is an important step forward conceptually for UTC to serve as a common time reference for Global Navigation Satellite System (GNSS) interoperability.

Preface

This thesis is an original work. No part of this thesis has been previously published. However, Chapters 6, 7, and 8 were co-written with Prof. Barry C. Sanders. These chapters are part of a draft manuscript that is ready for submission to a journal.

Acknowledgements

I would like to extend my deepest gratitude to my thesis advisor, Prof. Barry C. Sanders, for his constant support, insight, and encouragement. Your expertise has not only been invaluable in overcoming the obstacles faced in my research, but you have also fundamentally shaped the way I think and express myself, enabling me to communicate more clearly and concisely. This skill set has proven to be just as critical as any academic knowledge I have gained, and for that, I am profoundly thankful.

I am also indebted to the members of my supervisory committee, Profs. Christoph Simon and Daniel Oblak whose rigorous critiques have pushed me to refine my arguments. I would also like to express my gratitude to Prof. Claudia Gomes da Rocha for agreeing to be an examiner for my thesis defence.

I would like to thank my colleagues for the stimulating discussions and debates that have enriched my academic experience. Your insights were invaluable. I also owe a great deal to my friends, both within and outside the academic sphere. While you may not have contributed directly to my research, your companionship was essential for my well-being and focus throughout this journey.

Above all else, I must acknowledge my family, who are the bedrock upon which all my endeavors, academic or otherwise, are built. Mom, Dad, and my dear sister, Farnaz, you have provided endless love, encouragement, and a sense of grounding that transcends any scholarly milestone I could ever achieve. Your sacrifices and constant support have not only made this academic journey possible but have shaped me into the person I am today.

The gravity of your sacrifice weighs even more given the geographical distance that has separated us. Moving to Canada to pursue my studies was a daunting decision, yet you never let your personal feelings obstruct my path or make me feel guilty for choosing this route. Your selflessness in letting me go, to better myself, embodies a love that words cannot fully capture. My academic achievements are not the pinnacle of success; the true triumph is in knowing that your love and sacrifice exist independently of any achievements I could earn. I dedicate this work to you, but more importantly, I dedicate my life to honouring the incredible people you are.

Lastly, I cannot complete this acknowledgment without paying homage to the belief that underpins my existence, my faith in God. There was a point in my life when the fundamental question of "why we live" plagued me to no end. The answer came not from logic or worldly gains but from a profound faith in a Creator with a grander plan, a purpose, for each of us. While the specifics of that plan remain a mystery to me, the belief in an afterlife where I will better understand my true purpose fuels me to persevere through life's many challenges. In moments when existence seems devoid of meaning, it is this unshakable belief that reorients me, giving me the strength to continue. If there were nothing beyond this life, the struggles and triumphs here would seem pointless to me. But with faith, every obstacle overcome and every achievement gained takes on a dimension of significance that goes beyond the here and now.

For this divine sustenance, I am eternally grateful.

Contents

List of Figures and Illustrations

List of Tables

List of Symbols & Abbreviations

Symbol or abbreviation	Definition
BeiDou-3	Chinese satellite navigation system
BIPM	Bureau International des Poids et Mesures
DFT	Density Fourier Transform
ET	Ephemeris Time
EAL	Échelle Atomique Libre
GHZ	Greenberger–Horne–Zeilinger
GLONASS	Globalnaya Navigazionnaya Sputnikovaya Sistema
GMT	Greenwich Mean Time
GNSS	Global Navigation Satellite System
GPS	Global Positioning System
HL	Heisenberg Limit
LO	Local Oscillator
MJD	Modified Julian Date
NIST	National Institute of Standards and Technology
NRC	National Research Council
OU	Ornstein-Uhlenbeck
PPP	Precise Point Positioning
PPS	Pulse Per Second
PFS	Primary Frequency Standard
QEC	Quantum Error Correction
RTK	Real-time Kinematic
SDE	Stochastic Differential Equation
SI	International System of Units
TAI	International Atomic Time
TIC	Time Interval Counter
TWSTFT	Two-Way Satellite Time and Frequency Transfer
UT1	Universal Time
UTC	Coordinated Universal Time
UTC(k)	Local realization of UTC
WFN	White Frequency Noise
WSN	White Speed Noise
¶	Paragraph
§	Section

Chapter 1

Introduction

1.1 Background

Clocks

Timekeeping involves counting the oscillations of a periodic event. Historically, the Sun's movement was used, leading to the invention of sundials based on shadow tracking [1]. However, sundials do not work without sunlight, prompting the development of mechanical clocks such as the pendulum clock. In the 1580s, Galileo noticed that a pendulum took the same time to swing regardless of its arc's length, but he could not construct a clock based on this observation. In 1656, Huygens developed a pendulum clock with an error of less than 1 minute per day, which was later reduced to 10 seconds per day [2]. Later, in 1921, Shortt designed a unique clock with two pendulums—master and slave. Shortt's clocks were incredibly accurate, deviating only a second per year [3].

Despite the remarkable accuracy of pendulum clocks, their physical limitations and sensitivity to environmental factors soon became apparent. This led to new breakthroughs in timekeeping technology, notably by Marrison in 1928, who introduced a groundbreaking technique using quartz crystals. Marrison's quartz clocks outperformed the then state-of-the-art Shortt's pendulum clocks in stability and accuracy [4]. By the end of World War II,

quartz clocks had achieved remarkable stability, deviating by only a second over 30 years. Yet, even these advanced quartz clocks had their limitations; they were highly sensitive to environmental factors such as temperature [5].

The limitations of quartz clocks created the impetus for further advancements, setting the stage for the invention of atomic clocks in the 1950s. In 1967, the SI unit of the second was redefined as "the duration of 9 192 631 770 periods of the radiation corresponding to the transition between two hyperfine levels of the ground state of the caesium 133 atom. It was later clarified that this definition refers to an atom at rest at a thermodynamic temperature of 0 K" [6]. Unlike quartz clocks, atomic clocks exploit quantum mechanics, which dictates that atoms have discrete energy levels. An atom can transition between these levels by either absorbing or releasing energy. The frequency of this transition is related to the energy difference between the two levels [7]. However, even these highly stable atomic clocks are not without their challenges. The stability is influenced by a range of factors, including the dispersion of energy transition frequencies and the signal-to-noise ratio [8].

To better understand these challenges, one can look at one of the early attempts to create a reliable atomic clock. Lyons developed the first atomic clock at the US National Bureau of Standards (now NIST), using ammonia molecules instead of atoms for frequency reference [5]. This experimental system employed a quartz-crystal oscillator, syntonized with the ammonia's resonant frequency, to control a display device operating at a much lower frequency [9]. Despite its innovative design, ammonia-based atomic clocks suffered from stability issues, mainly due to molecular collisions and the Doppler effect, which broadened the absorption line [10]. Consequently, these clocks could maintain time to within only one second over thirty years, rendering them no more stable than existing quartz clocks or the Earth's rotation. Because of these limitations, they were not pursued further, and the search for more reliable atomic clocks continued.

It was in this context that, in 1955, Essen and Parry at the National Physical Laboratory developed the first thermal caesium beam clock [11]. Within a caesium-beam clock, heated

cesium atoms travel as a gas beam through a vacuum tube, interacting with magnets and a U-shaped Ramsey microwave cavity [7]. Only when the microwave frequency aligns with the caesium's resonance frequency does the atom's energy state change [9]. The atom's subsequent detection adjusts a quartz oscillator's frequency to match the cesium atom's hyperfine state transition frequency. cesium's characteristics, such as its atomic speed and high hyperfine frequency, make it an optimal choice for atomic clocks [12]. This new design effectively addressed challenges such as atom collisions and Doppler broadening that plagued ammonia-based clocks, achieving a fractional frequency stability that surpassed ammonia and quartz clocks by five orders of magnitude [12].

Despite these advancements, cesium clocks still had their limitations. One such limitation was that caesium clocks based on magnetic selection and detection were inefficient at utilizing atoms from the source, as many atoms were initially in the wrong state. Researchers had contemplated increasing the atom flux as a solution, but this approach had its own drawbacks [13]. The idea of optical pumping, first suggested by Kastler in 1950 but not fully utilized until the late 1990s, employs a laser to transition atoms to a preferred energy state [14], thereby ensuring that all atoms eventually reside in the desired state. This method also allows for state detection, achieving an impressive 100% detection efficiency [15]. Optically pumped cesium clocks have superior stability due to a higher number of state-selected atoms. Notably, the NIST-7 clock reached a fractional frequency stability of 5×10^{-15} [16].

While optically pumped cesium clocks like NIST-7 offered improved stability, they still had their own set of limitations. This led researchers to revisit an earlier concept: cesium fountain clocks, initially proposed in the 1950s [17]. These clocks became viable with the advent of laser cooling techniques and utilize optical molasses to drastically cool and slow down atoms [18]. A pivotal advancement is the extended Ramsey time (to be explained in §5.1), which allows these clocks to achieve an even more impressive fractional frequency stability of 10^{-16}, marking a significant leap over traditional optically-pumped clocks [19].

While cesium fountain clocks marked a significant advance in timekeeping technology,

they are not the most stable atomic clocks. Here, optical atomic clocks enter the arena. Operating at higher frequencies, these clocks offer further reductions in instability, making them superior even to the refined cesium fountain clocks [19]. These clocks utilize laser-cooled ions or neutral atoms. Traditional electronic devices were unable to measure optical frequencies until optical frequency combs came into play, bridging the gap between optical clocks and electronic counters [20]. For heightened stability, optical lattice clocks, which merge benefits from ion traps and neutral atoms, were developed [21]. These clocks can confine numerous neutral atoms, ensuring greater stability, and currently, the most advanced optical atomic clocks offer a fractional frequency stability two orders of magnitude superior to fountain clocks [22]. But how do we quantify this stability, and what fundamental limitations could theoretical physics impose on these advanced atomic clocks?

Quantum-enhanced atomic clocks

An atomic clock's stability is proportional to $1/\sqrt{N}$, where N is the number of atoms used as the frequency reference. The $1/\sqrt{N}$ is commonly referred to as the standard quantum limit (SQL) [23]. Any scaling better than $1/\sqrt{N}$ is an indication that quantum resources such as entanglement of the energy states of the N atoms are used. The best scaling is $1/N$, which is known as the Heisenberg limit and can be achieved for instance by using a maximally entangled state such as a GHZ state. The Heisenberg limit is the fundamental limitation in the stability of atomic clocks and cannot be surpassed [24]. But what happens when we consider decoherence?

Asymptotically ($N \to \infty$), regardless of the initial quantum state or the measurement approach, Markovian noise processes results only in a constant (i.e., N-independent) improvement in stability [25, 26, 27]. Stability enhancement by a factor of $N^{1/4}$ and $N^{1/3}$ might be possible for non-Markovian noise [28, 29] or noise perpendicular to the signal [30], respectively. However, the appropriate Ramsey time tends to zero for large N in the aforementioned cases. This reduction in Ramsey time cancels out the enhancement in N and

therefore, the stability is not enhanced. Fully functional quantum-enhanced atomic clocks are demonstrated experimentally [31, 32, 33]. These experiments did not surpass the stability of state-of-the-art fountain clocks due to the reduction in T_{R} compared to conventional clocks, validating the theoretically established concerns.

Given these inherent limitations, researchers have explored other methods for enhancing stability, such as quantum error correction, to see if they can break these barriers. Quantum error correction mitigates decoherence and restores the Heisenberg limit if the Hamiltonian does not lie in the span of Lindblad operators, a condition known as Hamiltonian-not-in-the-Lindblad-span (HNLS) [34]. Otherwise, the improvement is just a constant factor, even with the use of quantum error correction [35, 36, 34]. Unfortunately, the dephasing noise that dominates atomic clock performance [25, 37] is described by a Lindblad operator, and the Hamiltonian is trivially in the span of that operator. Therefore, atomic clock scaling limitation cannot be mitigated by quantum error correction.

Time scales

While the development of advanced clocks allows us to measure time intervals with incredible accuracy, understanding what those intervals represent in the grand scheme of timekeeping has been a historical challenge. Clocks simply specify a time interval, but cannot, on their own, determine an instant of time. An agent can establish a starting point to count the tick-tocks of the clock, thereby establishing a time scale that designates the timing of the events [38, 39]. Historically, celestial patterns, particularly the Sun's position, established time scales, leading to the creation of solar days [40]. However, solar days vary throughout the year. To solve this, mean solar time was developed, defining a second as $1/86400$ of a mean solar day, and establishing Universal Time (UT1) [41]. The 19^{th}-century rise of railways pushed for internationally coordinated time, with the Greenwich meridian becoming the prime meridian and the world being divided into time zones [42]. In the 20th century, it became clear that Earth's rotation around its axis is not stable. This led to the Ephemeris

Time (ET), which used Earth's orbit around the Sun [43]. However, for accuracy and convenience, the atomic second replaced the Ephemeris second in 1967, and by 1971, the international atomic time (TAI) was established [44].

This relentless quest for more accurate and coordinated timekeeping culminated in the development of our current global standard: Coordinated Universal Time (UTC) [6]. UTC is based on the atomic second and involves a complex computation. Specifically, the ALGOS algorithm calculates the Échelle Atomique Libre (EAL) by averaging the readings of about 450 atomic clocks [45]. TAI is then derived by steering the EAL frequency to primary frequency standards [46]. UTC is finalized by introducing leap seconds to TAI as needed and is published in the monthly Circular T [47]. This intricate system relies on a suite of algorithms to ensure the accuracy, reliability, and stability of the global time scale [48].

However, UTC has some limitations. Due to its monthly computation, UTC is not accessible in real-time and, due to the absence of a physical representation, is often termed a "paper time scale." For these reasons, the local realizations of UTC, known as UTC(k) are established, where k stands for the name of the local site [49]. The time offset between UTC and each UTC(k) is published monthly in the Circular T. Subsequent to the dissemination of Circular T, laboratories change the frequency of their UTC(k) to remove the last known time offset over a period of time. Such frequency changes are comparable with the inherent frequency fluctuations due to UTC(k)'s instability. Large frequency changes result in better accuracy, yet they compromise stability. Thus, the laboratories aim to find a balance between optimizing UTC(k)'s accuracy, while maintaining its stability [50].

1.2 Problem statement and approach

In this section, I state the problem that I am addressing in my thesis and the approach I am taking to solve it. User-level positioning accuracy can be enhanced by utilizing all visible Global Navigation Satellite System (GNSS) satellites rather than relying solely on satellites

from one constellation. For this to happen, interoperability is needed among different constellations, particularly in terms of time offset between various GNSS time scales. In 2017, the International Committee on GNSS recommended each GNSS broadcast the time offset between its time scale and a common reference time scale. UTC could serve as this universal reference time scale. Yet, the success of this method requires synchronisation between different UTC(k) [51], but different UTC(k) are imperfectly sychnronised with the amount of asynchronisation not yet reliably quantifiable. We aim to quantify asynchronisation reliably between different UTC(k). To achieve our aim, we construct a model for quantifying asynchronisation reliably between different UTC(k). Furthermore, we establish a mathematical description for our model and solve it in closed form.

In our model, we conceptualize a clock using the analogy of a curling stone gliding on frictionless ice. This stone, moving steadily across equally spaced intervals on the ice, represents a "tick-tock" every time it crosses two intervals, mirroring the oscillations of traditional clocks like pendulums or atomic clocks. By introducing environmental noise, we capture the essence of real-world clock frequency fluctuations, assessing stability based on the stone's position diffusion. We also delve into constrained ballistic clocks, where the stone's velocity can be adjusted to keep it in sync with a reference clock akin to keeping UTC(k) in sync with UTC. Further, we introduce a coupled network of these clocks, akin to the UTC network, where each stone's velocity is adjusted intending to align the position of each stone with the average position that is announced by a master.

Finally, we extend our model to the quantum case and examine the relative positions and entanglement of ballistic clocks, which is crucial in understanding the limitations and potential advantages of quantum entanglement in timekeeping.

1.3 Outlook

The thesis is organized as follows. In Chapter 2, I provide an overview of clocks chronologically. I begin with pendulum clocks, which were the first human-made stable clock. Then I discuss quartz clocks, which were the next significant development in timekeeping. I finish by discussing atomic clocks, upon which the present global time standard is based.

In Chapter 3, I provide an overview of the evolution of timescales, commencing from their establishment based on celestial movements to the advent of international atomic time (TAI). Then, I discuss Coordinated Universal Time (UTC), focusing on its establishment and algorithms used in the process. Next, I discuss UTC(k), which are real-time local approximations of UTC. Finally, I discuss the various methods to obtain the time differences between clocks around the globe, which are the necessary inputs for the ALGOS algorithm.

In Chapter 4, I describe the mathematical approach that is used to characterize the performance of atomic clocks. First, I define two important parameters, time and frequency deviation. I then explain the Allan deviation as a measure of clock stability. Finally, I explain how stochastic differential equations are used to model the performance of atomic clocks.

In Chapter 5, I discuss quantum-enhanced atomic clocks. I begin by discussing Ramsey method of separated oscillating fields, which is used in atomic clocks. Then I explain what exactly is the quantum advantage for atomic clocks. Finally, I discuss the limitations of quantum advantage in the presence of decoherence.

In Chapter 6, I present our approach to quantify asynchronization between different local representations of UTC reliably. I begin by discussing our model of clocks. Next, I describe our model of clocks mathematically. Finally, I describe how we solve the mathematical expressions. In Chapter 7, I present our main results. Finally, I discuss our results in Chapter 8 and conclude.

Chapter 2

Background on clocks

In this chapter, I provide an overview of clocks chronologically. I begin with pendulum clocks, which were the first human-made stable clock. Then we discuss quartz clocks, which were the next significant development in timekeeping. We finish by discussing atomic clocks, upon which the present global time standard is based.

2.1 Pendulum clocks

Timekeeping requires selecting a periodic event and counting its oscillations. Historically, the apparent motion of the Sun was often chosen as the periodic event for timekeeping. The earliest timekeeping methods involved keeping track of the shadow of a stick placed upright in the ground. This technique transformed into the sundials, which used markers on the shadow's path to divide the day into smaller intervals. However, sundials are useless in the absence of sunlight. As a result, mechanical clocks like pendulum clocks were invented [1].

The pendulum clock, a prominent timekeeper for centuries, facilitated the use of seconds. In the early 1580s, Galileo Galilei observed that it took the same amount of time for a pendulum to move through a large arc as a small arc. However, we know that only the linear domain pertains to this observation. Galileo could not build a clock from this discovery, as he was unable to maintain the pendulum in motion. In 1656, Huygens designed a pendulum

escapement for this purpose. The error of Huygens's clock was less than 1 minute per day and was later reduced to 10 seconds per day [2].

Now we turn our attention to the Shortt's clock, which offered unparalleled stability with an innovative design. Shortt invented a novel pendulum clock in 1921 that has two pendulums, a slave and a master. In the Shortt's clock, the master pendulum swings freely in a vacuum chamber, only disturbed once every 30 seconds by a gravity lever escapement to maintain its oscillation. The motion of the gravity lever subsequently transmits an electrical pulse to the slave pendulum, ensuring its synchronization with the master. Shortt's clocks kept time within a second per year [3].

2.2 Quartz clocks

In 1928, Marrison discovered a groundbreaking timekeeping method, based on quartz crystals, which replaced Shortt's pendulum clocks as the frequency standards. These crystals exhibit piezoelectricity, meaning they oscillate when subjected to an alternating voltage, and vice versa. When subjected to a voltage at its harmonic frequency, the crystal vibrates in resonance. By the culmination of World War II, the stability of quartz clocks had evolved to the point where they would only lose or gain a second over the span of three decades [4].

The crystal's exact size and shape determine its frequency. Therefore, no two quartz clocks have identical frequency. Quartz clocks are also prone to changes in the environment, particularly in temperature. These restrictions render them unfit for applications that demand higher stability. For such needs, atomic clocks are employed instead [5].

2.3 Atomic clocks

In this section, we discuss atomic clocks. We begin by a high level introduction on their emergence, operational principle, and factors that effect their stability. Then, we provide an overview of the ammonia clock, which marked the beginning of the atomic clocks' invention.

Next, we discuss thermal cesium beam clocks. Subsequently, we discuss the use of optical pumping in cesium clocks to enhance their stability. Then, we discuss cesium fountain clocks, an advancement over cesium beam clocks. Finally, we delve into optical clocks, which are the current aspiration for the new generation of atomic clocks.

The invention of atomic clocks dates back to the 1950s, and since then, a variety of these clocks have been developed. Since 1967, the International System of Units (SI) defines the second as "the duration of 9 192 631 770 periods of the radiation corresponding to the transition between two hyperfine levels of the ground state of the caesium 133 atom. It was later clarified that this definition refers to an atom at rest at a thermodynamic temperature of 0 K" [6].

Quantum mechanics principles establish that an atom's energies possess specific, distinct values. An electromagnetic field with a certain frequency has the ability to elevate an atom from one energy state E_1 to an excited one E_2. Conversely, an atom with a high energy state can descend to a lower state by releasing energy. An atomic clock's frequency ν_0 is

$$\nu_0 := \frac{E_2 - E_1}{h}, \tag{2.1}$$

where h is the Planck's constant [7].

Energy absorption or emission occurs within a narrow range around ν_0, rather than exclusively at ν_0. An atomic clock's instability is inversely proportional to ν_0 and directly proportional to the dispersion $\Delta\nu$ (linewidth) of absorption or emission frequencies. The instability of an atomic clock is commonly articulated as fractional frequency instability,

$$\sigma \propto \frac{\Delta\nu}{\nu_0}\frac{1}{\mathrm{SNR}}, \tag{2.2}$$

where SNR is the signal-to-noise ratio [8].

If the stability is limited by quantum projection noise and the atomic transition is driven

using Ramsey's method of separated fields, we can write

$$\sigma = \frac{1}{2\pi\nu_0\sqrt{NT_{\mathrm{R}}}}, \tag{2.3}$$

where N is the number of atoms and T_{R} is the Ramsey time [52]. Recurring references to Eq. (2.3) will be made throughout this section. I cover Ramsey's method of separated fields and quantum projection noise in details in §5.1.

Ammonia clock

Lyons, while working at the US National Bureau of Standards, now known as the National Institute of Standards and Technology (NIST), developed the first atomic clock, which utilized the ammonia molecule as opposed to an atom. The ammonia molecule is composed of three hydrogen atoms and one nitrogen atom (NH_3), arranged in a pyramidal shape with the nitrogen atom located at the apex and the hydrogen atoms forming the base. As depicted in Fig. 2.1, nitrogen has the potential to occupy either the apex or the base of an inverted pyramid. The aforementioned energy states of the ammonia molecule corresponding to a frequency of 23.87 GHz served as the frequency reference employed in the first atomic clock [5].

To harness the ammonia molecule's frequency for a clock, a feedback system employing a quartz-crystal oscillator and ammonia molecules is used. The quartz oscillator generates a frequency close to the ammonia's resonant frequency and is broadcast into an ammonia chamber. When the radio signal matches the resonant frequency, the ammonia molecules strongly absorb the signal. The absorption, inversely proportional to the difference between the radio signal and resonant frequency, is used to syntonize the quartz oscillator frequency with the ammonia's transition frequency. The quartz oscillator controls a display device like a wall clock, which runs at a lower frequency (e.g., 60 Hz). Electronic circuitry reduces the Quartz's frequency in a gear-like manner to achieve this lower frequency [9].

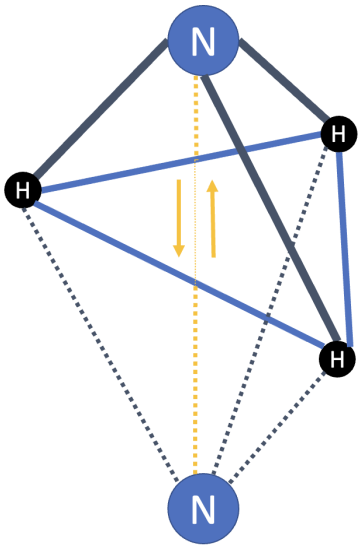

Figure 2.1: Ammonia molecule featuring a central nitrogen atom connected to three hydrogen atoms in a pyramidal arrangement. When exposed to microwaves of the appropriate frequency, the nitrogen atom flips through the triangular base formed by the hydrogen atoms, transitioning to a position below the pyramid. Dashed and solid lines represent the chemical bonds, while the orange line illustrates the nitrogen atom's path during the location change. Arrows indicate the up and down vibrational motion of the nitrogen atom in response to microwave radiation.

The construction of an atomic clock by stabilization on a molecular absorption, had significant stability limitations. Collisions and the Doppler effect contributed to a significant broadening of the absorption line ($\Delta\nu$ in Eq. (2.1) increases). The best ammonia clocks maintained time to within one second in thirty years [10]. Therefore, the stability of ammonia clocks was not better than that of quartz clocks or the earth's rotation around its axis and as a result, they were not further explored.

Cesium beam clocks

At the National Physical Laboratory (NPL), Essen and Parry pioneered the construction of the first thermal cesium beam clock in 1955 [11]. The valance electron of cesium atom acts like a magnet due to its spin. Concurrently, the cesium atom's nucleus has its own spin, culminating in the formation of an additional magnet. The interaction between these two magnets results in two distinct energy states: one characterized by the alignment of

the magnets north poles in the same direction, and another distinguished by their anti-parallel orientation. The difference between these energy states corresponds to a frequency of 9.192,631,770 GHz, which serves as the frequency reference for cesium clocks [9].

In a cesium-beam clock, cesium atoms are heated into a gas, forming a high-velocity beam travelling through a vacuum tube towards a pair of magnets. These magnets permit only one magnetic energy state to pass into a U-shaped Ramsey microwave cavity, exposing atoms to a microwave frequency derived from a quartz oscillator. Inside the cavity, separated microwave fields are applied to the atoms. The time between these separated fields is T_{R} in Eq. (2.3). The energy state of the atoms changes if the microwave frequency matches cesium's resonance frequency. Atoms then pass through another magnetic gate, with only state-changed atoms proceeding to a detector. The detector provides feedback, tuning the quartz oscillator's frequency to maximize state changes, thereby locking the oscillator's frequency to the hyperfine state transition frequency. Figure 2.2 illustrates the operation of cesium beam clocks [7].

Cesium possesses various characteristics that render it an ideal candidate for an atomic clock. Due to its atomic mass, cesium atoms move at approximately 130 $^{\mathrm{m}}/_{\mathrm{s}}$ at room temperature. This grants cesium atoms an extended T_{R} compared to hydrogen atoms, which travel around 1600 $^{\mathrm{m}}/_{\mathrm{s}}$ under the same conditions. Furthermore, cesium exhibits a high hyperfine frequency (represented by ν_0 in Eq. (2.3)) compare to other atomic oscillators, such as rubidium (roughly 6.8 GHz) and hydrogen (approximately 1.4 GHz) [12].

Cesium atoms moving as a beam without clashing into each other, effectively addresses one of the challenges associated with ammonia clocks. By directing the microwave signal perpendicular to the cesium beam, Doppler broadening, a further issue in ammonia clocks, is mitigated [9]. The fractional frequency stability of these cesium beam clocks reached the 10^{-14} level, five orders of magnitude higher than ammonia and quartz clocks [12].

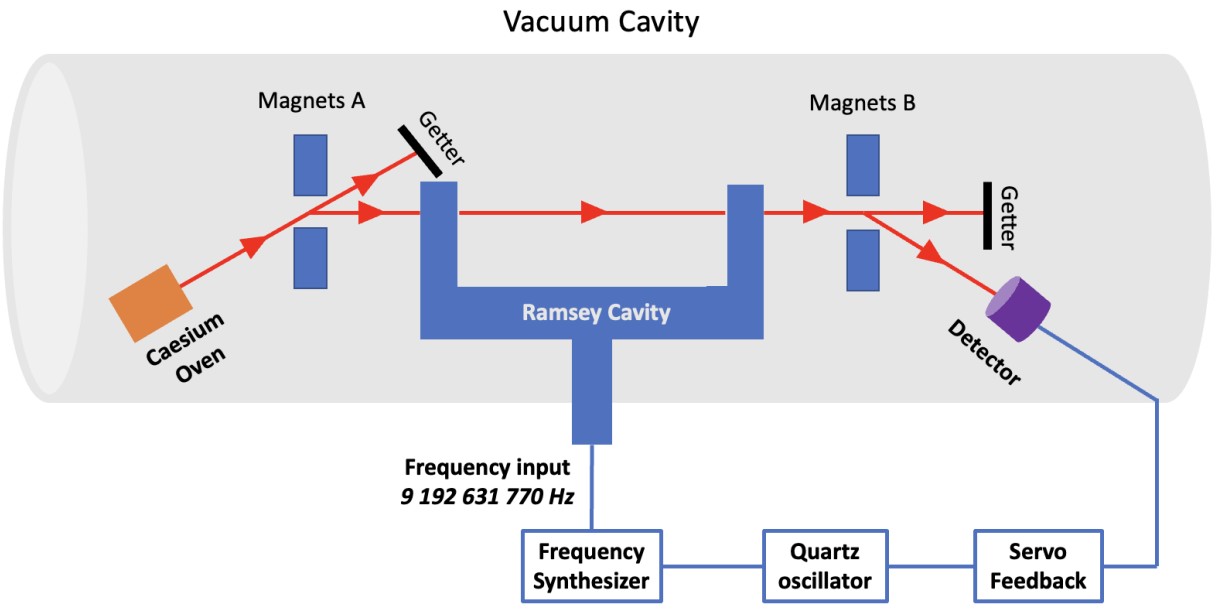

Figure 2.2: Schematic representation of a cesium beam clock. Key components include: a cesium oven (orange rectangle), atomic trajectory (red lines), state-selecting magnets (blue rectangles), getters (black narrow rectangles), Ramsey cavity (blue U-shaped structure), and detector (purple cylinder). The operational flow following cesium atom detection is illustrated by the blue lines.

Optically-pumped cesium beam clocks

Cesium clocks based on magnetic selection and detection, failed to efficiently use the atoms emerging from the source, as the majority of the atoms were in an incorrect state. This issue could be partially addressed by increasing the flux of atoms emanating from the source, but the attainable increase was constrained by the speed of atoms moving through the interaction region (resulting in a smaller T_{R} according to Eq. (2.3)) [13].

Kastler proposed using optical pumping as an alternative to the state-selection magnet in cesium beam clocks as early as 1950 [14]. Optical pumping is a technique that transfers all atoms into a preferred state. This is achieved by stimulating the atoms from state A to an optically meta-stable excited state C using a laser tuned to the transition frequency. Atoms in state C then return to either state A or the preferred state B in about 30 ns, with approximately equal likelihood. Atoms that revert to state B no longer interact with the laser and remain inactive, while those returning to state A are re-excited until they

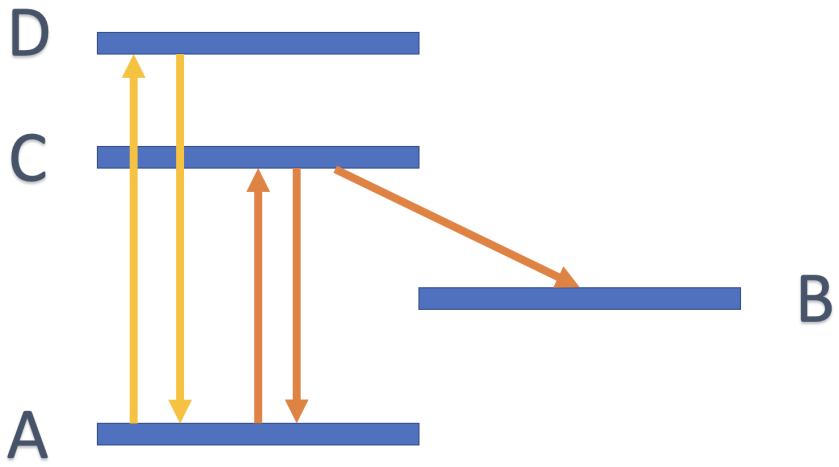

Figure 2.3: Depiction of energy levels pertinent to optical state preparation and detection. Allowed transitions are represented by arrows, with orange arrows denoting optical pumping for atomic preparation in state B, and yellow arrows indicating the cyclic transition employed for atom detection.

eventually decay to state B, ensuring all atoms ultimately reside in the desired state B [53].

Optical methods can also be employed for state detection. This is accomplished by pumping from state A to state D, where atoms can only decay back to state A. This process is known as a cycling transition. By leveraging such a transition, a single atom can scatter a substantial number of photons (or fluorescent), thereby achieving a detection efficiency of 100% [15]. Figure 2.3 illustrates the relevant energy levels.

Optically pumped cesium clocks exhibit increased stability as a result of a larger quantity of state-selected atoms, which in turn improves the signal-to-noise ratio in Eq. (2.2). Devices of this nature were operational in the late 1990s and ultimately delivered a fractional frequency stability just under 10^{-14}. NIST-7, the final atomic beam clock developed at NIST, achieved a stability of 5×10^{-15} due to the implementation of optical pumping [16].

Cesium fountain clocks

Cesium fountain clocks were developed to address the shortcomings of cesium beam clocks due to the high-speed of atoms and the resulting short T_{R}. The initial idea for a cesium

fountain was proposed in the 1950s by Zacharias as a vertical cesium beam clock with a single Ramsey interaction zone, through which atoms would pass twice, first ascending and then descending under the influence of gravity. This idea, however, did not work at the time and was only revisited when laser cooling and trapping techniques made it possible to capture a large number of atoms (in the tens of millions) at low thermal velocities, resulting in a longer T_{R} [17].

Optical molasses, a laser cooling method, is typically employed in fountain clocks. This method applies a damping force to atoms using three pairs of counter-propagating lasers (Fig. 2.4 adopted from [18]). The lasers are set to a frequency just below the atoms' optical resonance. At the intersection of the six laser beams, atoms are cooled to a temperature below $1\,\mu$K within tenth of a second. Similar to moving through a viscous substance like molasses, the cooled cesium atoms decelerate to approximately $1\,{}^{\mathrm{cm}}/_{\mathrm{s}}$, which enables a cluster of atoms to be contained in one place [18].

To throw the atoms upwards, the frequencies of the vertical lasers are detuned from one another so that the atoms are launched at a speed of roughly $4\,{}^{\mathrm{m}}/_{\mathrm{s}}$. Optical pumping prepares the atoms in the desired state, akin to optically-pumped clocks. The atoms travel upwards and downwards through the microwave resonator. After passing through the microwave resonator for the second time, the state's population is measured using laser irradiation and fluorescence detection, again resembling optically-pumped clocks. The T_{R} is approximately 1 s, an improvement of about 100 times compared to beam clocks [54, 21]. The fractional frequency stability of the best cesium fountain clocks is 10^{-16} [19], which is over an order of magnitude more stable than optically-pumped clocks like NIST-7.

Optical clocks

Optical atomic clocks incorporate frequencies (ν_0 in Eq. (2.2)) that are about five orders of magnitude greater than microwave clock, with comparable linewidth ($\Delta\nu$ in Eq. (2.2)). Therefore, optical clocks can significantly reduce the instability. Optical clocks rely on laser-

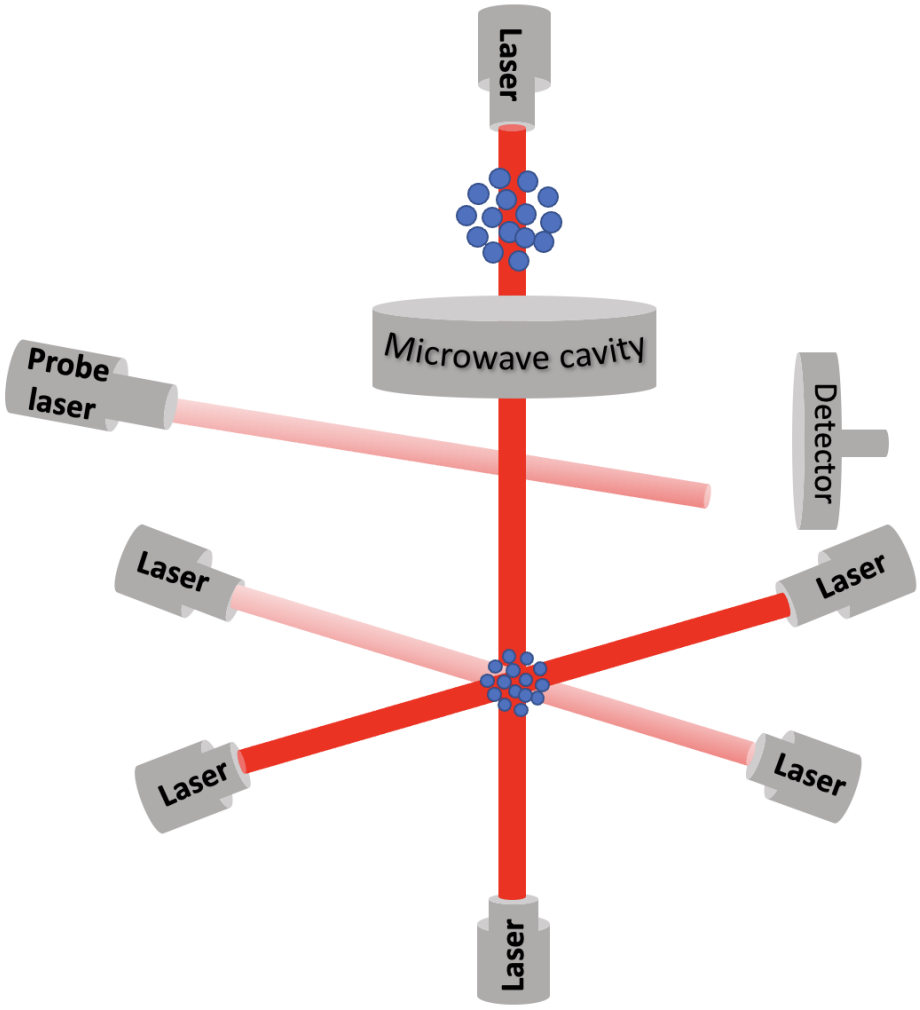

Figure 2.4: Schematic representation of a fountain clock, with key components labelled. Notably, red narrow cylinders denote laser beams, and small circles represent atoms. The increased spacing between atoms at the top signifies their dispersion as they ascend.

cooled ions or neutral atoms and require three key components: a stable local oscillator (LO), an optical transition, and a frequency counting mechanism. The LO is a highly stable laser, while the atomic reference or clock transition involves a weak, forbidden optical transition. Lastly, a femtosecond laser frequency comb serves as the frequency counting mechanism [19].

The inability of conventional electronic devices to measure optical frequencies hindered the development of optical clocks until the advent of optical frequency combs. A frequency comb is produced using ultrafast, mode-locked lasers, which emit a series of very short pulses. In the frequency domain, these pulses are seen as a series of equally spaced and sharp frequency peaks, resembling a comb's teeth. Serving as a bridge between optical clocks and electronic counters, frequency combs enable precise frequency measurements by acting as a frequency ruler. The frequency of optical clocks is determined by measuring the beat frequency between the local oscillator (LO) and the nearest comb tooth [20].

The optical clocks that rely on ions utilize only one ion to eliminate the possibility of collisions between ions. However, having just one ion ($N = 1$) can lead to a low stability in Eq. (2.3). To overcome this issue, optical lattice clocks are developed. Optical lattice clocks combine the advantages of both ion traps and neutral atoms. By trapping a large number of neutral atoms (large N in Eq. (2.3)), a higher stability can be achieved, and similar to ion traps, neutral atoms trapped in the optical lattice allows for long T_{R} [21]. The best optical atomic clocks have a fractional frequency stability in the order of 10^{-18}, two orders of magnitude better than fountain clocks [22].

Chapter 3

Background on time scales

In this chapter, I provide an overview of the evolution of timescales, commencing from their establishment based on celestial movements to the advent of international atomic time (TAI). Then, I discuss Coordinated Universal Time (UTC), focusing on its establishment and algorithms used in the process. Next, I discuss UTC(k), which are real-time local approximations of UTC. Finally, I discuss the various methods to obtain the time differences between clocks around the globe, which are the necessary inputs for the ALGOS algorithm.

3.1 History of time scales

Clocks simply specify a time interval, but cannot, on their own, determine an instant of time. An agent can establish a starting point to count the tick-tocks of the clock, thereby establishing a time scale that designates the timing of the events [38, 39].

Throughout history, people have favoured using celestial movements as a way to establish time scales. The time of day has been determined by solar time in some way since ancient times. Solar time is based on the Sun's position in the sky. As Earth rotates around its axis, the Sun appears to move across the sky. Solar noon is when the Sun is directly overhead. The duration between one solar noon and the following one is considered a solar day. A time scale based on Earth's rotation around its axis can thus be established by picking a starting

point and then counting the cycles from one solar noon to the next [40].

Due to the fact that the Earth's orbit around the Sun is not a perfect circle, and the fact that the Earth's axis is tilted relative to its orbit, the length of a solar day can vary slightly throughout the year. On the other hand, mean solar time is like finding the middle ground between all the different solar days that happen throughout the year. Mean solar time is based on a hypothetical mean Sun that moves in a way so that each mean solar day is exactly 24 hours long. The mean Sun replaced our actual Sun because it was more stable. The definition of second was also based on the mean solar day. A second was $^1/_{86400}$ of a mean solar day. The time scale based on the mean solar time is called the Universal Time (UT1) [41].

With the development of railways in the 19th century, there was a need for a unified time scale between countries. Some nations had based their official time on a specific meridian. In 1884, a crucial step was taken toward establishing a global time scale. A prime meridian was selected, and a Universal Time was established based on the mean solar time of this prime meridian. The world was then separated into 24 time zones, each separated by one hour. The initial time zone was based on the prime meridian, which was the Greenwich meridian. This marked the beginning of internationally coordinated time, with nations adopting legal times that corresponded to their respective time zones [42].

It is essential to understand that Greenwich Mean Time (GMT) and the Universal Time (UT1) are not the same. Greenwich Mean Time begins at noon, when the Sun is directly above the Greenwich meridian, whereas UT1 begins at midnight. The Universal Time has replaced Greenwich Mean Time as the standard time for civil purposes. Despite the fact that this change occurred decades ago, many people continue to incorrectly use the term GMT when they mean UT1 [55].

Astronomers have long believed that the rate of Earth's rotation is constant. However, scientists realized in the 1930s that this is not the case. Astronomers sought a more stable clock to establish a more stable time scale. The second was redefined as $^1/_{31,556,925.9747}$ of

the 1960 tropical year. The tropical year is the time required for the Earth to complete a single rotation around the Sun and return to the vernal equinox (when the Sun is directly above the equator). Therefore, the new clock depicted the Earth orbiting the Sun rather than rotating on its axis. The time scale based on the rotation of Earth around the Sun is called the Ephemeris Time (ET) [43].

When ET was first proposed, it was only meant for scientific purposes, while UT1 was still used by the general public. However, determining Ephemeris Time was inconvenient and not accurate. Eventually, the Ephemeris second was replaced by the atomic second as the standard unit of time in 1967 and a new time scale called the international atomic time (TAI) based on atomic clocks was established in 1971 [44].

3.2 Coordinated Universal Time (UTC)

Despite TAI's designation as the primary time scale, Coordinated Universal Time (UTC) has become the practical world time reference. UTC was picked due to its ability to approximate the Universal Time. UTC is based on the atomic second, the same as TAI, but it is adjusted to maintain a difference from the Universal Time of less than 0.9 seconds. This is accomplished by adding or subtracting leap seconds to keep UTC in sync with the Earth's rotation. Currently, the offset between TAI and UTC is 37 seconds [6].

A time scale intended use determines its requirements, and for a worldwide time scale like UTC the requirements are accuracy, reliability, and stability [48]. Accuracy is that the period matches the definition of the second as closely as possible, the reliability is no counts are missed, and the stability is to preserve the counting rhythm. One clock and an agent are sufficient to realize a time scale, but to improve reliability and stability, a clock network is used [46].

To generate UTC [45], first, The ALGOS algorithm is used to calculate the Échelle Atomique Libre (EAL) by taking a weighted average of 450 clocks, although the exact

CIRCULAR T 410 ISSN 1143-1393
2022 MARCH 11, 10h UTC

BUREAU INTERNATIONAL DES POIDS ET MESURES
THE INTERGOVERNMENTAL ORGANIZATION ESTABLISHED BY THE METRE CONVENTION
PAVILLON DE BRETEUIL F-92312 SEVRES CEDEX TEL. +33 1 45 07 70 70 tai@bipm.org

The contents of the sections of BIPM Circular T are fully described in the document "Explanatory supplement to BIPM Circular T" available at https://webtai.bipm.org/ftp/pub/tai/other-products/notes/explanatory_supplement_v0.6.pdf

1 - Difference between UTC and its local realizations UTC(k) and corresponding uncertainties.
From 2017 January 1, 0h UTC, TAI-UTC = 37 s.

Date 2022 0h UTC	JAN 30	FEB 4	FEB 9	FEB 14	FEB 19	FEB 24	Uncertainty/ns			Notes
MJD	59609	59614	59619	59624	59629	59634	uA	uB	u	
Laboratory k	[UTC-UTC(k)]/ns									
AGGO (La Plata)	423.9	450.5	469.5	469.5	466.5	484.1	1.0	20.0	20.0	
AOS (Borowiec)	-6.4	-6.7	-6.4	-6.5	-6.1	-5.5	0.3	3.1	3.1	
APL (Laurel)	3.3	1.3	0.4	0.0	0.0	-0.2	0.3	19.7	19.7	
AUS (Sydney)	-543.2	-527.1	-523.2	-527.8	-519.0	-526.0	0.3	11.2	11.2	
BEV (Wien)	67.5	66.6	56.4	42.2	37.1	23.0	0.3	2.6	2.6	(1)
BFKH (Budapest)	4181.1	4215.1	4249.8	4283.4	4309.0	4338.0	1.5	20.0	20.1	
BIM (Sofiya)	15770.4	15783.2	15817.0	15818.7	15834.8	15890.8	0.3	7.1	7.1	
BIRM (Beijing)	11.3	9.4	8.0	7.1	5.7	5.3	0.3	3.0	3.0	
BOM (Skopje)	-813.2	-993.0	-	-	-	-	0.3	3.5	3.5	
BY (Minsk)	0.6	0.4	0.0	-0.3	-0.1	-0.6	1.5	2.8	3.2	

Figure 3.1: Part of Circular T for February 2023.

number varies from month to month. Next, The International Atomic Time scale (TAI) is established by steering the EAL frequency to primary frequency standards to ensure the accuracy of the time scale. Finally, by adding leap seconds to TAI, UTC is computed and made accessible on paper as [UTC − UTC(k)] in a monthly publication of Circular T [47] at 5-day intervals as shown in Fig. 3.1.

ALGOS algorithm

Here, I explain the ALGOS algorithm, without delving into details within the main portion of the thesis. Additional information can be found in Appendix A.

EAL is [6]

$$\mathrm{EAL}(t) := \sum_{i=1}^{N} w_i \left[h_i(t) + h_i'(t) \right], \tag{3.1}$$

where N represents the total number of atomic clocks, w_i indicates the relative weight of clock H_i, $h_i(t)$ denotes the reading of clock H_i at time t, and $h_i'(t)$ is the prediction of clock H_i's reading to ensure a continuous time scale (refer to Appendix A for details).

In practice, data is not derived from direct clock readings. Instead, data is obtained from

time differences between clocks, expressed as

$$x_{i,j}(t) := h_j(t) - h_i(t). \tag{3.2}$$

We can restate Eq. (3.1) using $x_{i,j}(t)$ as follows

$$\mathrm{EAL}(t) - h_j(t) = \sum_{i=1}^{N} w_i \left[h'_i(t) - x_{i,j}(t)\right]. \tag{3.3}$$

As a result, the time difference between any clock H_j and EAL is contingent upon weights, clock predictions, and clocks' time differences. Clock H_j could also symbolize a UTC(j) time scale, in which case, $\mathrm{EAL}(t) - h_j(t)$ could be understood as $\mathrm{EAL}(t) - \mathrm{UTC}(k_j)(t)$, with k_j standing for the name of the site j.

Prediction algorithm

Consider two successive intervals of EAL calculation, $I_{k-1}(t_{k-1}, t_k)$ and $I_k(t_k, t_{k+1})$. The term $h'_i(t)$ ensures that EAL, its first derivative (frequency of EAL), and its second derivative (frequency drift of EAL) are continuous at t_k. The prediction term $h'_i(t)$ can be expressed as the following [56]

$$h'_{i,I_k}(t) := \hat{x}_{i,I_k}(t_k) + \hat{y}_{i,I_k}(t - t_k) + \frac{1}{2}\hat{C}_{i,I_k}(t_k - t_{k-1})(t - t_k) + \frac{1}{2}\hat{C}_{i,I_k}(t - t_k)^2. \tag{3.4}$$

Now I explain each term. First, $\hat{x}_{i,I_k}(t_k)$ is

$$\hat{x}_{i,I_k}(t_k) := \mathrm{EAL}_{I_{k-1}}(t_k) - h_i(t_k) := x_{i,I_{k-1}}(t_k), \tag{3.5}$$

is the time difference between EAL in the previous interval and the reading of clock H_i at $t = t_k$. Second, $\hat{y}_{i,I_k}$ is

$$\hat{y}_{i,I_k} := \frac{x_{i,I_{k-1}}(t_k) - x_{i,I_{k-1}}(t_{k-1})}{t_k - t_{k-1}}, \tag{3.6}$$

is the normalized frequency deviation between clock H_i and EAL in the previous interval. Finally, C_{i,I_k} is our estimation of the normalized frequency drift deviation between clock H_i and EAL. The calculation of this quantity involves comparing the frequency of the clocks to a reference time scale, TT(BIPM), standing for Terrestrial Time as realized by BIPM [6].

Weighting algorithm

The weighting algorithm follows a four-iteration process with each iteration runs as follows [57]

(1) The values $x_{i,I_k}(t)$ are found using a given set of w_i. In the first iteration, the weights come from the prior calculation interval after normalization. In subsequent iterations, they come from the previous iteration.

(2) The absolute difference between the actual mean frequency deviation y_{i,I_k} and the predicted mean frequency $\hat{y}_{i,I_k}$ obtained by Eq. (3.6) is represented by

$$\epsilon_{i,I_k} = |y_{i,I_k} - \hat{y}_{i,I_k}| \,. \tag{3.7}$$

(3) The square of Eq. (3.7) is calculated for each clock.

(4) One year's worth of ϵ_{i,I_k} is taken into account to ensure the long-term stability of EAL and UTC.

(5) A filter has been put in place to prioritize recent measurements over older ones, with the assumption that newer measurements have more reliable statistics

$$\sigma_i^2 = \frac{\sum_{j=1}^{M} \left(M+1-j/M\right) \epsilon_{i,j}^2}{\sum_{j=1}^{M} M+1-j/M}, \tag{3.8}$$

where i denotes the clock, j signifies the calculation interval, and M represents the

number of available measurements (ranging from 5 to 12 since 5 months is the minimum observation period for a clock before incorporating it into the UTC calculation, and one year is the standard observation period).

(6) The relative weight of clock H_i is determined using a temporary value given by

$$w_{i,\text{temp}} = \frac{1/\sigma_i^2}{\sum_{i=1}^{N} 1/\sigma_i^2}. \tag{3.9}$$

The weight w_i of clock H_i is equal to $w_{i,\text{temp}}$ with two exceptions:

(a) If $w_i > w_{\max} = 4/N$, then $w_i = w_{\max}$.

(b) If clock H_i shows abnormal behaviour, i.e., if $|y_{i,I_k} - \hat{y}_{i,I_k}| > 5\,\text{ns}/\text{day}$, then $w_i = 0$.

For more details on the evolution of the weighting algorithms, please refer to Appendix B.

Steering algorithm

The stability of UTC is maintained through the employment of prediction and weighting algorithms. A select group of metrology labs has developed a few primary frequency standards to ensure UTC's accuracy. TAI utilizes the SI second as its scale interval, which is derived from the hyperfine transition of the cesium atom as determined by these primary frequency standards (PFSs). To elaborate, the first step involves establishing the EAL using the aforementioned algorithms. Following this, EAL's frequency is compared to the primary frequency standards, and a frequency steering correction is applied to guarantee UTC's frequency aligns with its definition [58].

Laboratories responsible for upkeeping primary frequency standards provide the International Bureau of Weights and Measures (BIPM) with measurements of the primary standard's frequency in relation to EAL over a specific time frame where the standard has been in operation more or less continuously (typically between 10 and 30 days). BIPM's algorithm for estimating TAI's scale unit duration [59] fuses individual PFS calibrations and computes the

time scale's frequency during a designated interval (usually the month in which Circular T is calculated) [60].

For a frequency standard denoted as j, there are n_j calibrations performed. When considering N standards, the total number of calibrations available is represented by $\sum_{j=1}^{N} n_j$. The EAL frequency over a specified time interval T can be determined using the formula

$$y = \sum_{j=1}^{N} \sum_{i=1}^{n_j} a_{ji} W_{ji}, \tag{3.10}$$

where W_{ji} signifies the difference in frequency between EAL and frequency standard j for a specific interval T_{ji}. Meanwhile, a_{ij} denotes the filter coefficients, which are influenced by factors such as the uncertainty of evaluation i for standard j and the distance between T_{ji} and T [45].

3.3 UTC(k)

A consequence of UTC's monthly computation is the inability to determine the time for a month, necessitating real-time UTC approximations through the establishment of UTC(k) time scales. Consequently, real-time UTC is accessible only via these local approximations [49]. The time offset between UTC(k) and UTC, denoted as [UTC − UTC(k)], is reported monthly in the BIPM Circular T [47]. Each UTC(k) employs one or more continuously operating, free-running atomic clocks. Operating multiple atomic clocks within a laboratory offers protection against the failure of any individual clock. Furthermore, a time scale derived from a collection of clocks can exhibit improved stability compared to a single clock [49].

To establish UTC(k), the time differences between clocks are measured with respect to a reference clock, and a weighted average of the data is defined as a time scale known as TA(k). Subsequently, leap seconds are incorporated, resulting in what I like to call TAL(k), which represents TA(k) adjusted for leap seconds. One can envision a master clock within the

laboratory that realizes TAL(k). To obtain UTC, the master clock's frequency is adjusted to align its time with UTC and the output of this clock realizes UTC(k) [50].

TAL(k) can be conceptualized as a free-running clock, as it is not guided towards any reference clock. Conversely, UTC(k) is considered a coupled clock, as its time is directed towards UTC. To achieve this coupling, laboratories first examine their time offsets relative to UTC following the publication of Circular T. Subsequently, they modify UTC(k)'s frequency to eliminate the time difference over a specified duration [50]. For instance, if UTC(k) trails UTC by 10 ns, the frequency of UTC(k) is momentarily adjusted to gain 2 ns per day, eradicating the time difference over a 5-day period.

One might wonder why laboratories do not instantaneously implement a time step to eliminate the time offset. The objective is to eradicate the time offset without compromising UTC(k)'s frequency stability. As a result, the magnitude of frequency change should be constrained to a value comparable to UTC(k)'s instability-induced frequency fluctuations. An immediate time step corresponds to a substantially larger frequency change, adversely impacting UTC(k)'s stability. However, the quicker the time offset is removed (increasing coupling strength), the more accurate UTC(k) becomes relative to UTC. Consequently, a trade-off exists between enhancing UTC(k)'s accuracy and maintaining its frequency stability [50].

3.4 Time comparison methods

Calculating UTC using clocks from different labs necessitates comparing distant clocks without affecting their stability. Previously, time comparison methods often limited timescale construction. The BIPM establishes an international time link network, utilizing a star-like scheme that connects all the labs to a pivot lab, currently housed at the Physikalisch-Technische Bundesanstalt (PTB) in Germany. Due to the use of various time comparison methods by different labs, pivots are chosen from those with continuous operation of all

methods. This allows for pivot changes if the needs arise [6].

GPS common view and all in view method

Until 2006, the GPS common view method was a popular technique for comparing distant clocks [6, 61]. In this method, both clocks simultaneously receive signals from the same GPS satellite. At each clock location, agents record signal arrival times t_{a_1} and t_{a_2}. The time taken for the GPS signal to travel from the satellite to each clock is calculated by dividing distances d_1 and d_2 by the speed of light c. Agents then subtract these travel times from arrival times to determine transmission times t_{T_1} and t_{T_2}. Finally, the time difference between the two clocks is calculated by subtracting the transmission times.

In the GPS common view method, both receivers track a common GPS satellite simultaneously. However, as the distance between the two clocks being compared increases, the chances of finding a common high-elevation satellite for both receivers diminish. As a result, the time difference measurements may be affected by lower signal-to-noise ratio and less accurately known propagation delays, which can degrade the overall accuracy of the GPS common view method. This is why the GPS all-in-view method, has been developed. In the GPS all-in-view method, both receivers simultaneously track all visible GPS satellites (not necessarily in common view), and the time difference is calculated based on the weighted average of the measurements from all satellites [62].

GPS receivers can track two types of measurements: code measurements and carrier phase measurements. Code measurements are relatively simple to process. Carrier phase measurements track the phase of the carrier signal, which requires more complex signal processing and data handling. Despite the increased complexity, carrier phase measurements offer several advantages over code measurements such as two orders of magnitude higher precision, less sensitivity to multipath, and better estimation of atmospheric effects. GPS Precise Point Positioning (PPP) is a method that analyzes satellite signals by combining both carrier phase and code measurements [63]. GPS all-in-view method combined with

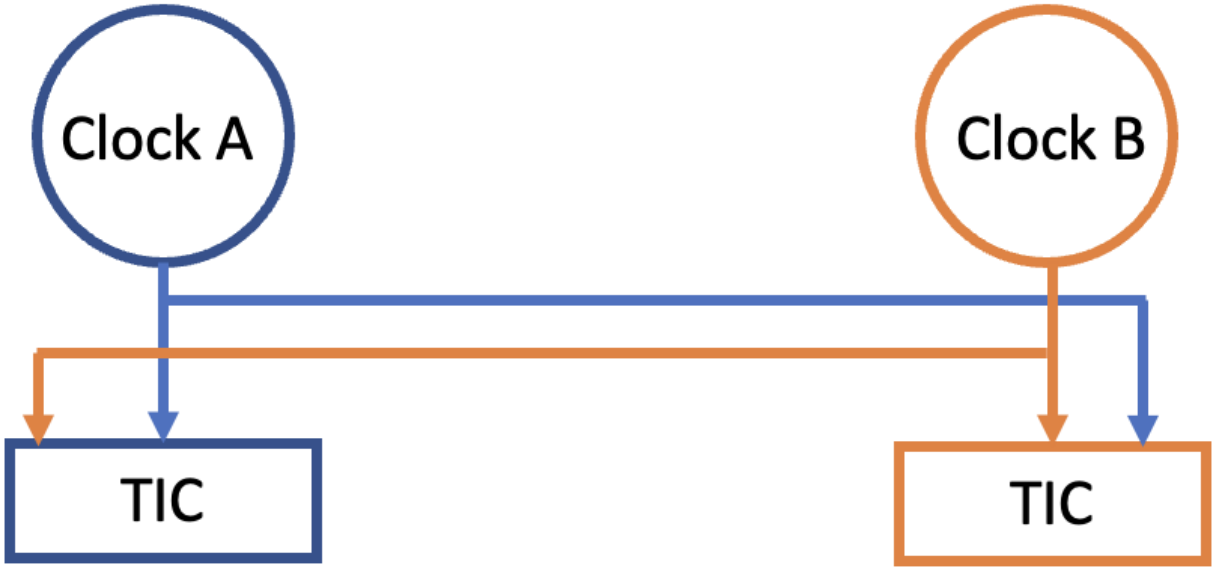

Figure 3.2: Schematic depiction of two way time comparison. The directional flow of 1 PPS signals emitted from Clock A and B are highlighted by blue and orange arrows, respectively.

GPS PPP is the most popular method of time comparison in UTC [64].

Two-Way Satellite Time and Frequency Transfer (TWSTFT)

TWSTFT is a method for comparing two distant clocks by simultaneously exchanging signals via a geostationary telecommunications satellite. The two-way time transfer technique (without satellite) is illustrated in Fig. 3.2 [65]. The technique involves two clocks (A and B) and two time interval counters (TICs). The left TIC measures the difference between the 1 pulse per second (PPS) from clock A and clock B with cable delay t_{BA}, while the right TIC measures the difference between clock B and A with cable delay t_{AB}. The time difference between the two clocks is determined by

$$t_A - t_B = \frac{R(A) - R(B)}{2} + \frac{t_{AB} - t_{BA}}{2}, \tag{3.11}$$

where $R(A)$ and $R(B)$ are the TICs readings [65].

In instances where the two clocks are situated at significant distances precluding the use

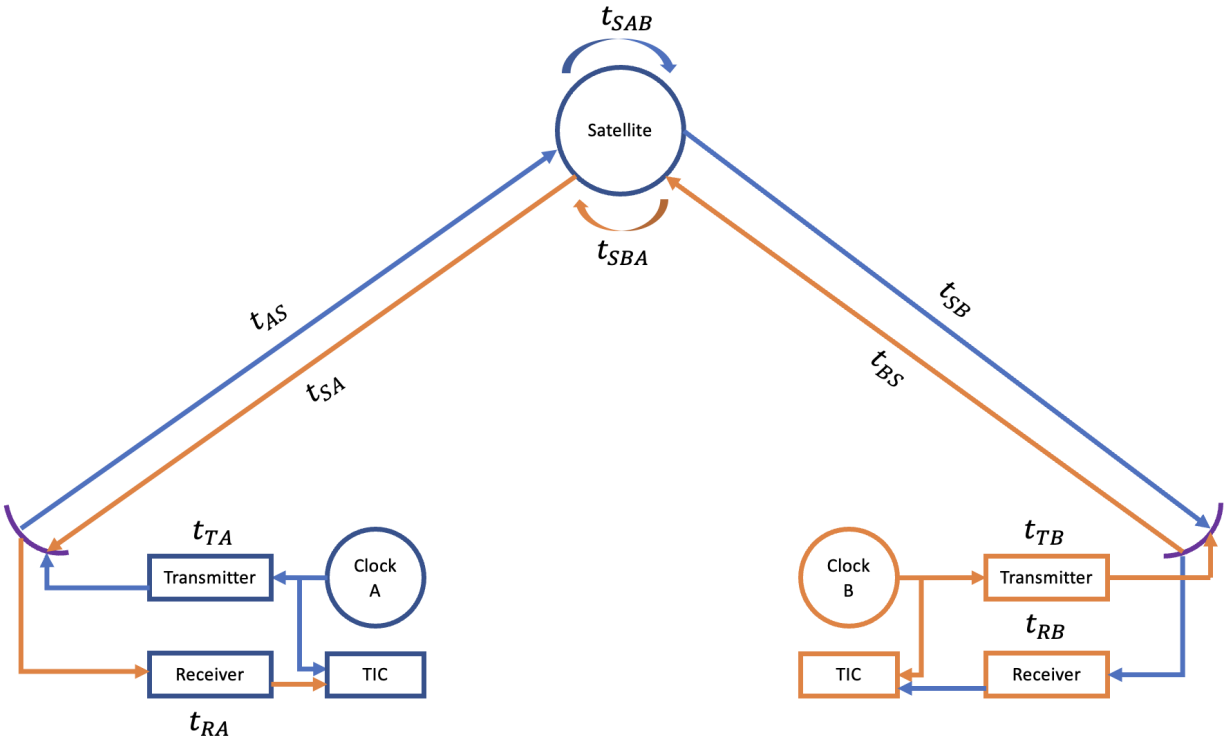

Figure 3.3: Schematic representation of TWSTFT. Blue and orange arrows indicate the directional flow of 1 PPS signals from Clock A and B, respectively. Antennas are represented by purple semicircles. Time delays associated with the transmitter, receiver, and signal transit between transmitters and satellite, as well as between satellite and receiving station, are illustrated within the diagram.

of cables, satellite-assisted transmission is employed to convey the timing signals. Satellite-based time comparison resembles the cable method but requires accounting for additional delays. These delays encompass those associated with the transmitter and receiver, the signal transit time between the transmitter and satellite as well as between the satellite and the receiving station, and the effects of Earth's rotation. A comprehensive illustration of the essential components of TWSTFT technique can be found in Fig. 3.3 [65]. Figure 3.4 provides a schematic overview of UTC calculation.

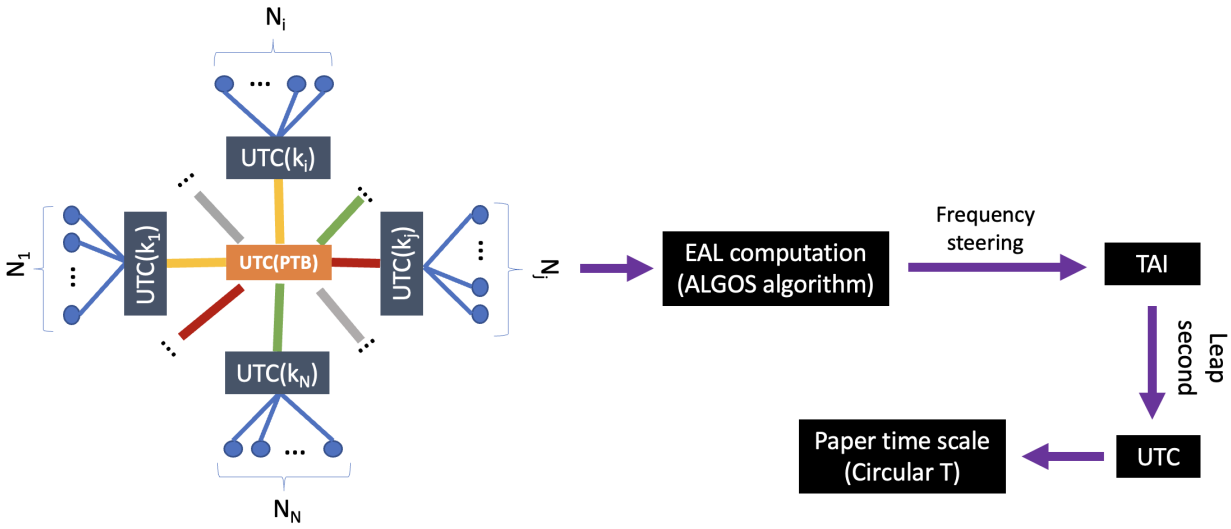

Figure 3.4: Schematic overview of the UTC calculation process. Blue circles denote individual clocks within each laboratory, with N_1, N_i, N_j, and N_N indicating the number of clocks utilized per lab. Blue lines illustrate comparisons between laboratory clocks and a master clock realizing UTC(k), shown by UTC(k) inside the rectangles. Colored thin rectangles convey dual meanings: comparison of all UTC(k) with UTC(PTB) and representation of distinct time comparison methods, such as All in view or TWSTFT. Purple arrows depict the computational flow for UTC, beginning with the submission of $x_{i,j}$ values to BIPM for EAL calculation.

Chapter 4

Background on mathematical characterisation of atomic clocks

Here I describe the mathematical approach that is used to characterize the performance of atomic clocks. First, I define two important parameters, time and frequency deviation. Then, I explain the Allan deviation as a measure of clock stability. Finally, I explain how stochastic differential equations are used to model the performance of atomic clocks.

4.1 Time & Frequency deviation

An ideal clock functions as an oscillator, generating a sinusoidal signal [66]

$$U(t) = U_0 \sin(2\pi\nu_0 t), \tag{4.1}$$

where U_0 represents the amplitude and ν_0 the frequency of oscillation. If we introduce the ideal clock reading

$$h_0(t) \equiv t \tag{4.2}$$

then Eq. (4.1) transforms to

$$U(t) = U_0 \sin\left[2\pi\nu_0 h_0(t)\right]. \tag{4.3}$$

In real-world scenarios, however, clocks are seldom ideal.

For a noisy clock, both amplitude and frequency are subject to random fluctuations. However, the amplitude fluctuations can be considered negligible

$$U(t) = U_0 \sin\left[2\pi\nu_0\left(t + \frac{\phi(t)}{2\pi\nu_0}\right)\right], \tag{4.4}$$

where $\phi(t)$ denotes the effect of frequency fluctuations on the phase of the signal. We define the reading of a noisy clock as

$$h(t) \equiv t + \frac{\phi(t)}{2\pi\nu_0}, \tag{4.5}$$

which, after applying Eq. (4.2), becomes

$$h(t) = h_0(t) + \frac{\phi(t)}{2\pi\nu_0}. \tag{4.6}$$

Equation (4.6) mixes the reading of an ideal clock with the perturbations introduced by the frequency fluctuations.

Time deviation $x(t)$ is defined as the difference between the readings of an ideal and a noisy clock, meaning

$$x(t) := h(t) - h_0(t) = \frac{\phi(t)}{2\pi\nu_0}. \tag{4.7}$$

By definition, the instantaneous frequency of Eq. (4.4) is [67]

$$\nu(t) := \frac{1}{2\pi}\frac{\mathrm{d}}{\mathrm{d}t}\left[2\pi\nu_0\left(t + \frac{\phi(t)}{2\pi\nu_0}\right)\right] = \nu_0 + \frac{\dot{\phi}(t)}{2\pi},\ \dot{\phi}(t) = \frac{\mathrm{d}\phi(t)}{\mathrm{d}t}. \tag{4.8}$$

Another essential quantity for characterizing atomic clocks is the normalized frequency deviation,

$$y(t) := \dot{x}(t). \tag{4.9}$$

From Eqs. (4.8) and (4.9), we deduce that

$$y(t) = \frac{\nu(t) - \nu_0}{\nu_0}, \tag{4.10}$$

which is a significant parameter to assess the performance of atomic clocks as discussed in the next section.

4.2 Allan deviation

The instantaneous frequency deviation $y(t)$, as defined in Eq. (4.9), is not directly observable because any frequency measurement technique necessitates a finite averaging time τ for the measurement process. Instead, the observable quantity is the average frequency deviation $\bar{y}(t)$,

$$\bar{y}(t) := \frac{1}{\tau}\int_t^{t+\tau} \mathrm{d}t'\, y(t') = \frac{x(t+\tau) - x(t)}{\tau}. \tag{4.11}$$

To perform a statistical analysis, multiple measurements of $\bar{y}(t)$ are required [67].

An essential attribute of an atomic clock is its frequency stability, which can be intuitively understood as the reciprocal of the time variability of $\bar{y}(t)$. To establish frequency stability, we could potentially estimate the variance $\sigma^2(t)$ of $\bar{y}(t)$

$$\sigma^2(t) = \left\langle [\bar{y}(t) - \langle \bar{y}(t) \rangle]^2 \right\rangle, \tag{4.12}$$

where $\langle\rangle$ signifies a time average

$$\langle \bar{y}(t) \rangle = \lim_{T\to\infty} \frac{1}{T}\int_{-T/2}^{T/2} \mathrm{d}t\, \bar{y}(t). \tag{4.13}$$

A fundamental issue arises immediately: the noise impacting $\bar{y}(t)$ could exhibit a random walk characteristic, and the variance of a random walk is time-dependent. Furthermore, the variance not only changes over time but also diverges to infinity. Consequently, if we utilize

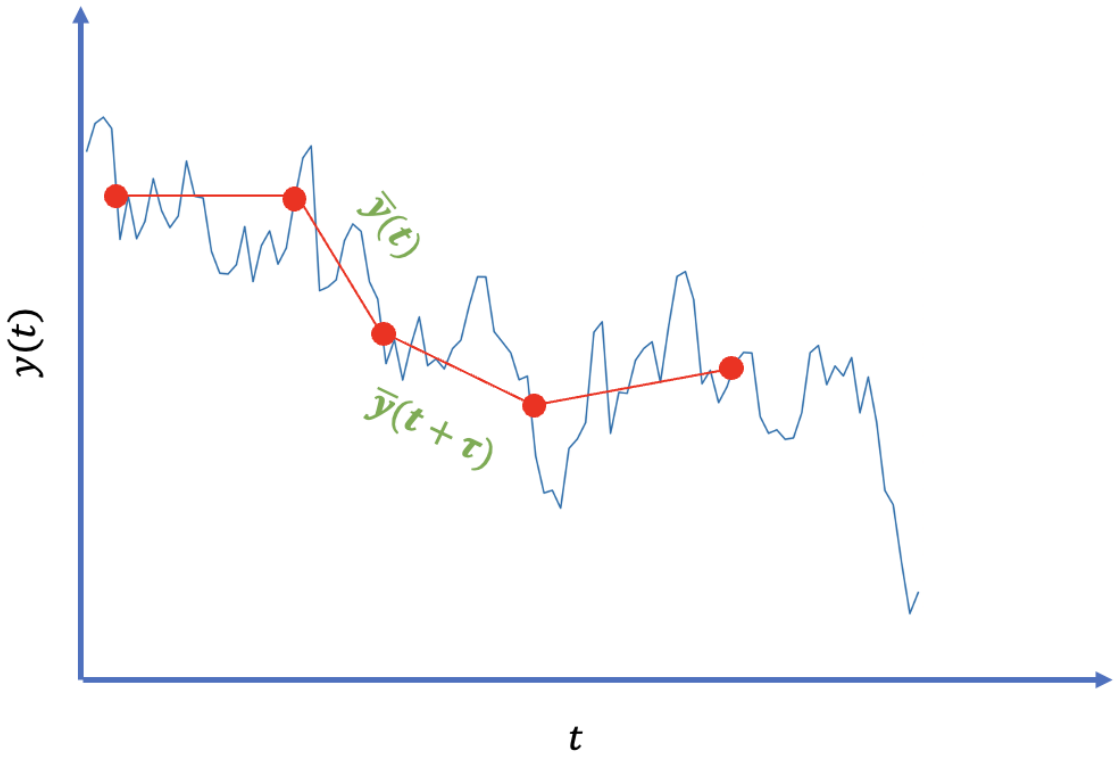

Figure 4.1: Illustration of the process for estimating average frequency deviations based on frequency deviation values.

variance as an indicator of stability, we obtain differing results based on the length of the time series [68].

The idea involves estimating the variance of the increments of $\bar{y}(t)$ values rather than the variance of the values themselves. It has been experimentally observed that the increments have stationary statistical properties. As a result, the variance of the increments no longer depends on the length of the time series. This method is employed in the definition of Allan variance

$$\begin{aligned} \sigma_y^2(\tau) &:= \frac{1}{2}\left\langle [\bar{y}(t+\tau) - \bar{y}(t)]^2 \right\rangle \\ &= \frac{1}{2\tau^2}\left\langle [x(t+2\tau) - 2x(t+\tau) + x(t))]^2 \right\rangle . \end{aligned} \tag{4.14}$$

The average frequency deviation $\bar{y}(t)$ can be determined either from the frequency deviation values (Fig. 4.1) or from the time deviation $x(t)$ values (Fig. 4.2) [69].

The Allan variance corresponds to the conventional variance when dealing with white

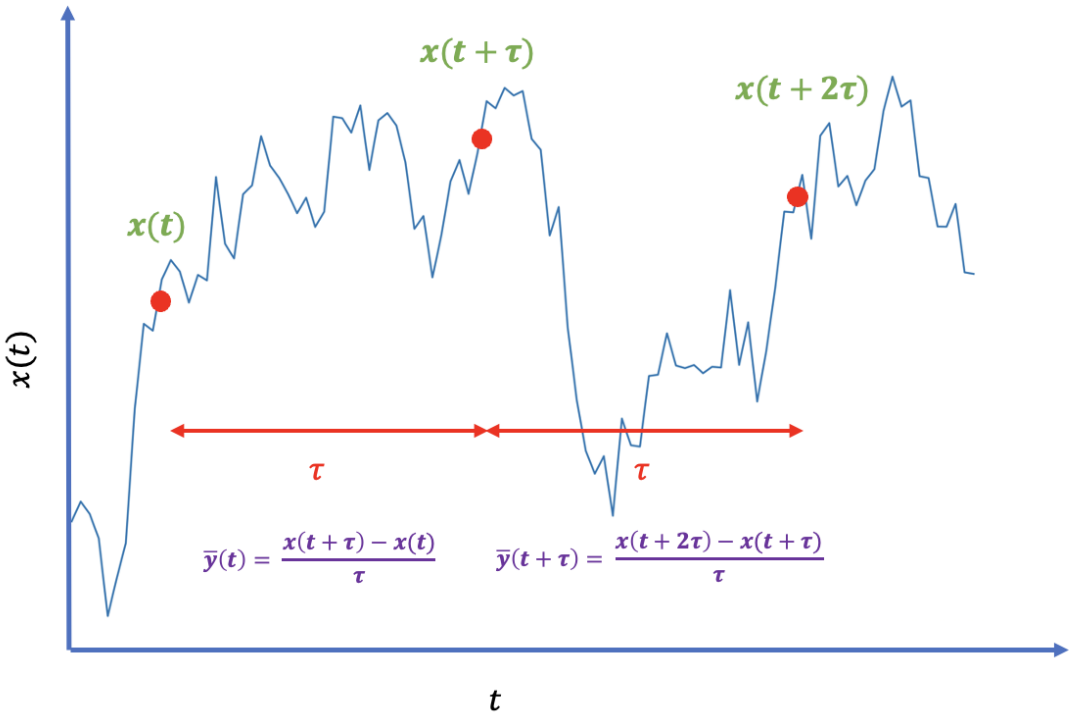

Figure 4.2: Estimation of average frequency deviations from the time deviation values.

frequency noise. This is anticipated since the issue with standard variance arises from the utilization of deviations from the mean, which is non-stationary exclusively for non-stationary noise types. White noise, on the other hand, is stationary. As such, the Allan variance offers an advantage when addressing non-stationary noise types such as random walk frequency noise. In these situations, the Allan variance converges to a value independent of the time series length, unlike the ordinary variance [70].

The Allan variance exhibits a power-law relationship given by

$$\sigma_y^2(\tau) = b_\mu \tau^\mu, \tag{4.15}$$

where b_μ represents a constant. Consequently, when $\sigma_y^2(\tau)$ is plotted as a function of τ on a log-log scale, it exhibits a slope of μ. Figure 4.3 demonstrates such a plot. As illustrated in the figure, the slope of $\log \sigma_y^2(\tau)$ varies within different τ ranges, depending on the noise type.

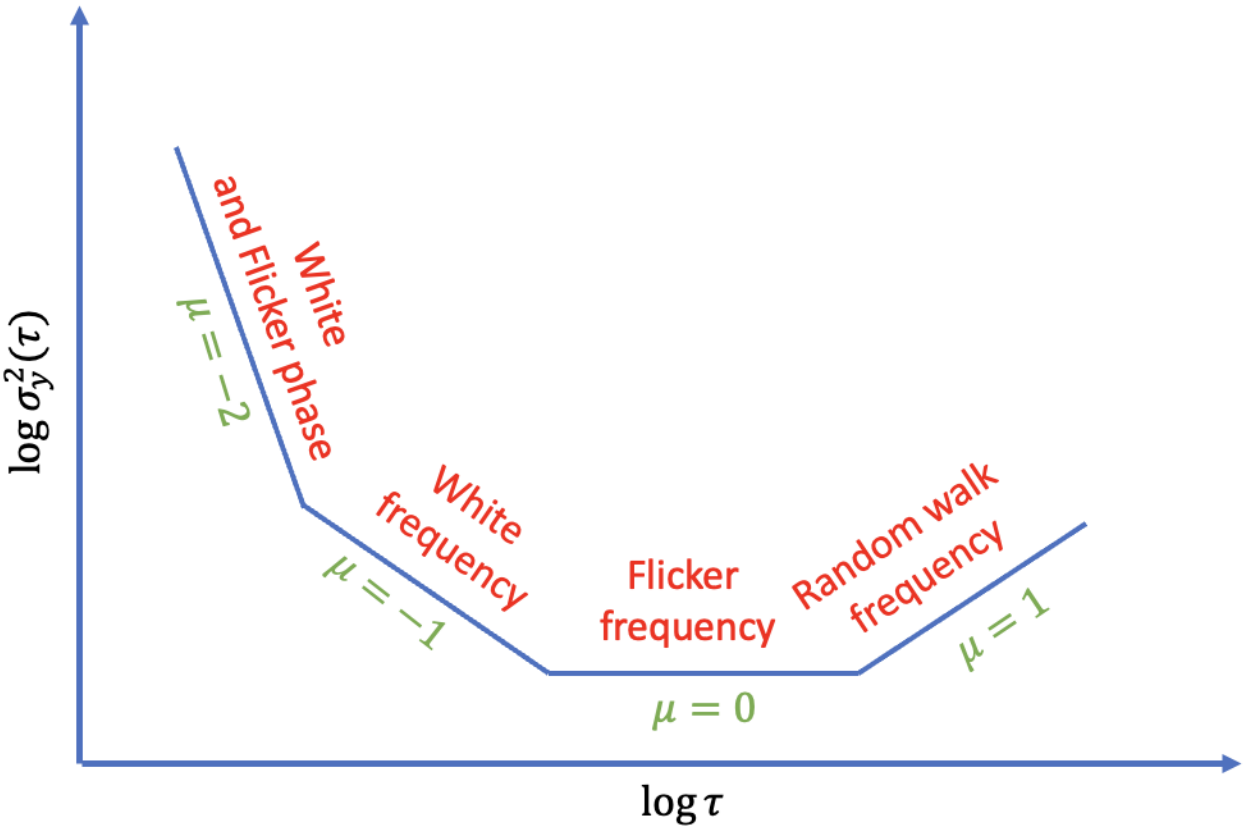

Figure 4.3: Log-log representation of Allan variance in relation to averaging time for typical atomic clock noise types.

Hence, assessing the slope of the Allan variance in relation to the averaging time on a log-log plot allows for the determination of the noise type [71]. The Allan variance, as defined in Eq. (4.14), necessitates an infinite time average. However, in practical scenarios, the infinite time average requirement is unattainable, and the Allan variance for finite averaging time or data points is approximated by [72]

$$\sigma_y^2(\tau) \cong \frac{1}{2(M-1)} \sum_{k=1}^{M-1} \left(\bar{y}_{k+1} - \bar{y}_k\right)^2 , \tag{4.16}$$

where M represents the number of $\bar{y}_k$ data points, and the subscript k indicates measurements taken at time t_k, $t_{k+1} = t_k + \tau$, $t_{k+2} = t_{k+1} + \tau$, etc. Combining Eqs. (4.11) and (4.16),

Eq. (4.16) can also be expressed in terms of time-deviation measurements

$$\sigma_y^2(\tau) \cong \frac{1}{2(N-1)\tau^2} \sum_{k=1}^{N-2} \left(x_{k+2} - 2x_{k+1} + x_k\right)^2, \tag{4.17}$$

where N denotes the number of x_k data points [73].

Since Eqs. (4.16) and (4.17) serve as approximations for the true Allan variance, they inherently possess uncertainty. The estimation uncertainty of the Allan variance is proportional to $1/\sqrt{M}$. Consequently, when τ spans days or even months, the limited number of data points poses a challenge in maintaining estimation uncertainty at the desired level for these extended averaging times. To address this issue, an alternative version of Allan variance, known as overlapping Allan variance, has been employed. A comprehensive explanation of this variance can be found in the cited reference [74], although we will not delve into the details here.

Importantly, Allan variance does not account for the dead time that occurs between average frequency measurements. Dead time refers to intervals between time-ordered data sets when no measurement of average frequency deviation is recorded. Ignoring dead time in the calculation of $\sigma_y^2(\tau)$ can lead to biased instability values, except in the case of white frequency noise. As such, $\sigma_y^2(\tau)$ should not be employed to describe these biased measurements without acknowledging the associated bias. Given that $x(t)$ can be routinely measured, it is preferable to utilize $x(t)$ for computing $\sigma_y^2(\tau)$, as this approach addresses the issue of dead time [75].

In order to illustrate the process of calculating Allan deviation, an example is provided in which $\sigma_y(\tau)$ is determined for $\tau = 1\text{s}$ and $\tau = 2\text{s}$. Tables 4.1 and 4.2 present the relevant data and steps for computing $\sigma_y(1\text{s})$ and $\sigma_y(2\text{s})$, respectively. Employing Eq. (4.16) for both calculations yields

$$\begin{aligned} \sigma_y(1\text{s}) &= 1.1 \times 10^{-12} \\ \sigma_y(2\text{s}) &= 8.9 \times 10^{-13}, \end{aligned} \tag{4.18}$$

t_k(s)	x_k(ps)	$\bar{y}_k = \frac{x_{k+1}-x_k}{\tau_0} \times 10^{12}$	$(\bar{y}_{k+1} - \bar{y}_k) \times 10^{12}$	$(\bar{y}_{k+1} - \bar{y}_k)^2 \times 10^{24}$
0	0	—	—	—
1	0.4	0.4	—	—
2	1.1	0.7	0.3	0.09
3	1.4	0.3	-0.4	0.16
4	3.3	1.9	1.6	2.56
5	3.2	-0.1	-2	4
6	4.1	0.9	1	1
7	4.0	-0.1	-1	1
8	1.3	-2.7	-2.6	6.76
9	1.9	0.6	3.3	10.89
10	1.6	-0.3	-0.9	0.81
11	2.8	1.2	1.5	2.25
12	3.9	1.1	-0.1	0.01
13	3.2	-0.7	-1.8	3.24
14	3.3	0.1	0.8	0.64
15	4.0	0.7	0.6	0.36
16	4.7	0.7	0	0

Table 4.1: Calculation steps for σ_y(1s). The first column represents time steps separated by 1s ($\tau_0 = 1$s). The second column displays corresponding time deviations in picoseconds. The third column contains the average frequency deviations derived from time deviations. The fourth column lists differences between neighbouring average frequency deviations. Lastly, the fifth column presents the squared values of these differences.

t_k(s)	x_k(ps)	$\bar{y}_k = \frac{x_{k+1}-x_k}{2\tau_0} \times 10^{12}$	$(\bar{y}_{k+1} - \bar{y}_k) \times 10^{12}$	$(\bar{y}_{k+1} - \bar{y}_k)^2 \times 10^{24}$
0	0	—	—	—
2	1.1	0.6	—	—
4	3.3	1.1	0.6	0.36
6	4.1	0.4	-0.7	0.49
8	1.3	-1.4	-1.8	3.24
10	1.6	0.2	1.6	2.56
12	3.9	1.2	1	1
14	3.3	-0.3	-1.5	2.25
16	4.7	0.7	1	1

Table 4.2: Calculation steps for σ_Y(2s). This table follows the same structure as table. 4.1, with the distinction that time steps are separated by 2s rather than 1s.

which shows the reduction of $\sigma_y(\tau)$ as τ increases.

4.3 Stochastic differential equations

Now we explain how stochastic differential equations (SDEs) are used to predict the performance of atomic clocks. We focus on two different clocks. First, a free running clock. Second, a coupled clock. Initially, we outline the dominant type of noise that perturbs the cesium clocks' frequency deviation and examine its impact on the time deviation. Subsequently, we formulate the SDE that describes the time-deviation fluctuation. Lastly, we delve into the relation between the SDE parameters and the Allan deviation.

Wiener Process

Now we discuss the dominant noise in cesium clocks. Experiments indicate that white frequency noise dominates the frequency deviation of a cesium clock for averaging times of up to 10 days [66]. Therefore, a (Gaussian-noise) Wiener process

$$\{W(t); t \geq 0\},\ W(0) = 0,\ W(t) \sim \mathcal{N}(0, t), \tag{4.19}$$

with $\sim \mathcal{N}(0, t)$ denoting a normal distribution with zero mean and variance t and $\sim$ denoting "is distributed as" [76] properly represents $x(t)$ (4.9) for a cesium clock [77]. The covariance of a Wiener process is

$$\operatorname{cov}\left(W(t)W(s)\right) := \min(t, s), \tag{4.20}$$

and since the mean of Wiener process is zero, the auto-correlation function, $\langle W(t)W(s)\rangle$, is equal to the covariance.

Free running clock

We now discuss how SDEs are used to indicate inaccuracy in synchronization in the case of a free running clock. The SDE that represents the dynamic of time deviation of a free running clock with the diffusion coefficient σ is [69]

$$\mathrm{d}x(t) = \sigma \mathrm{d}W(t). \tag{4.21}$$

The formal solution assuming $x(0) = 0$ (no initial time deviation) is

$$x(\tau) = \sigma \int_0^\tau \mathrm{d}W(t) \sim \mathcal{N}\left(0, \sigma^2 \tau\right), \tag{4.22}$$

which means,

$$\sigma_x(\tau) = \sigma\sqrt{\tau}. \tag{4.23}$$

Equation (4.23) indicates synchronization inaccuracy of a clock with respect to a reference clock after a prior synchronization [78].

OU process

Before delving into the modelling of a constrained clock, it is essential to understand the Ornstein-Uhlenbeck (OU) process. The OU process is a type of stochastic process that is particularly useful for modeling systems exhibiting mean reversion. Mathematically, it is expressed as

$$\mathrm{d}x(t) = -\kappa \left[x(t) - \mu\right] \mathrm{d}t + \sigma \mathrm{d}W(t), \tag{4.24}$$

where κ is the mean-reversion rate, μ is the mean, and σ is the diffusion coefficient. This process is characterized by its tendency to revert to its mean μ over time, making it distinctly different from processes like the Wiener process, which lack this mean-reverting property.

Constrained clock

Equation (4.24) is used to describe a constrained clock such as a steered clock which is constrained by a frequency action that forces $x(t)$ back towards μ [79]. Therefore, κ is the inverse of the time period it takes for $x(t)$ to reach μ, with μ an externally provided parameter. The case where $\kappa \to 0$ describes a free-running atomic clock (4.21).

We set $\mu = 0$ to ensure no time deviation between the noisy clock and the perfect one. In this case, the formal solution is

$$x(t) = \sigma \int_0^\tau \mathrm{d}W(t)\, \mathrm{e}^{-\kappa(\tau - t)} \sim \mathcal{N}\left(0, \frac{\sigma^2}{2\kappa}\left(1 - \mathrm{e}^{-2\kappa\tau}\right)\right), \tag{4.25}$$

which means

$$\sigma_x(\tau) = \sigma\sqrt{\frac{1}{2\kappa}\left(1 - \mathrm{e}^{-2\kappa\tau}\right)}. \tag{4.26}$$

Equation (4.26) illustrates the synchronization inaccuracy of the noisy clock with respect to the perfect clock to which it is coupled.

Diffusion coefficient and Allan deviation

We now discuss the connection between the Allan deviation and the diffusion coefficient. SDEs represent clock noise with diffusion coefficients, while Allan deviation is the usual way to characterize clock noise in time and frequency analysis. To effectively utilize the mathematical models for clocks, it is crucial to obtain the relations between the Allan deviation and the diffusion coefficient of both the Wiener process and OU process [80].

For a free-running clock, the relationship between the diffusion coefficient and the Allan deviation is [81]

$$\sigma_y(\tau) = \frac{\sigma}{\sqrt{\tau}}. \tag{4.27}$$

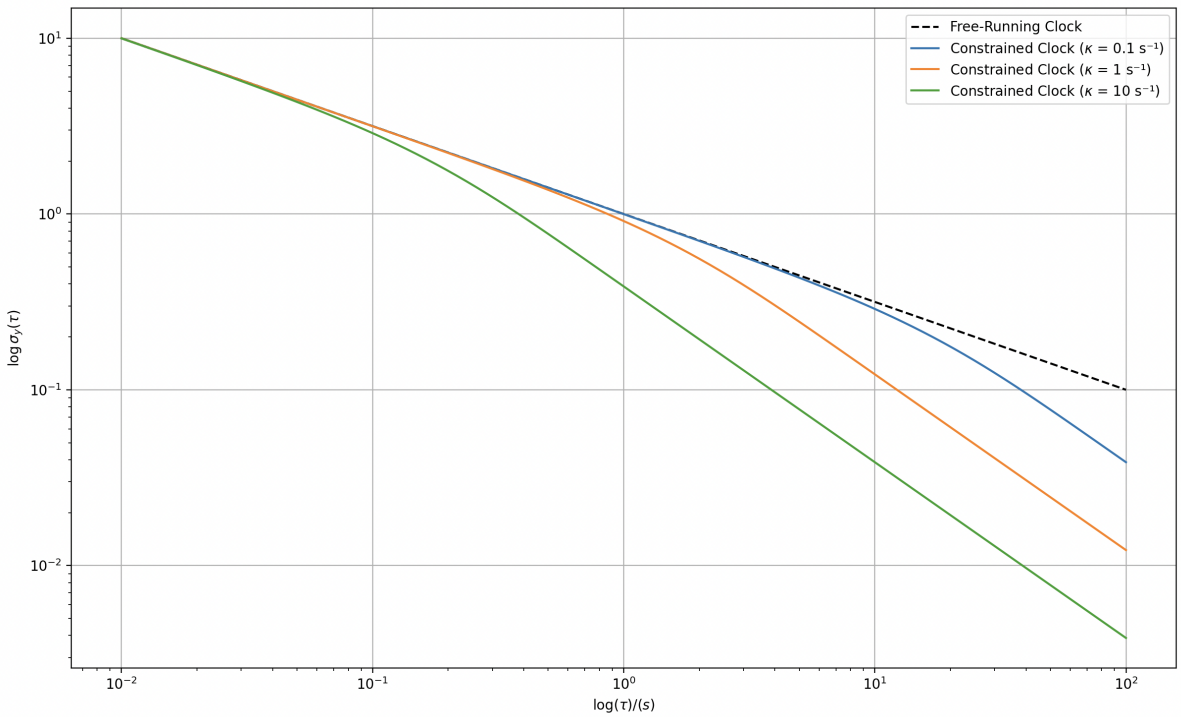

Figure 4.4: log-log plot of Allan deviation with respect to the averaging time for different coupling strengths. The diffusion coefficient is taken to be 1 $\sqrt{\text{s}}$.

and for a coupled clock, the relationship is [79]

$$\sigma_y(\tau) = \frac{\sigma}{\tau}\sqrt{\frac{1}{2\kappa}\left(3 - 4\mathrm{e}^{-\kappa\tau} + \mathrm{e}^{-2\kappa\tau}\right)}. \tag{4.28}$$

Figure 4.4 shows how the log of the Allan deviation changes with $\log(\tau)$ for different κ. You can see that for short averaging times the constrained clock behaves as a free-running clock, which is expected since Eq. (4.28) reduces to Eq. (4.27) when $\kappa\tau \ll 1$. However, the Allan deviation for the constrained clock is evidently smaller than the free-running clock, which is also expected since Eq. (4.28) scales as $1/\tau$ for $\kappa\tau \gg 1$. Furthermore, it is evident from the figure that higher coupling strength results in better stability in the long run.

Chapter 5

Background on quantum-enhanced atomic clocks

Here, we discuss quantum-enhanced atomic clocks. We begin by discussing Ramsey method of separated oscillating fields, which is used in atomic clocks. This will eventually help us to understand where $\sqrt{NT_{\mathrm{R}}}$ in Eq. (2.3) originates from which in turn prepare us to understand what exactly is the quantum advantage for atomic clocks, which is the subject of discussion in §5.2. Finally, in §5.3, I discuss the limitations of quantum advantage in the presence of decoherence.

5.1 Ramsey method of separated oscillating fields

The Ramsey method of separated oscillating fields (henceforth referred to as the Ramsey method) is employed in atomic clock frequency measurements, as outlined by Eq. (2.1). First, §5.1 aims to explain the concept without incorporating mathematics. Following this, a mathematical approach is introduced in §5.1, which serves to elucidate the genesis of the $\sqrt{NT_{\mathrm{R}}}$ component present in Eq. (2.3). This mathematical treatment also establishes the foundational understanding for future discussions on quantum-enhanced atomic clocks in §5.2.

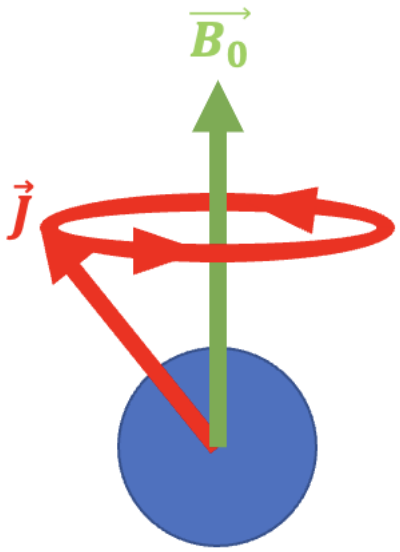

Figure 5.1: Schematic representation of Larmor precession. The blue circle indicates the electron. The red arrow indicates the direction of the spin angular momentum showed by the vector $\vec{J}$. The green arrow shows the direction of the external magnetic field showed by the vector $\vec{B}_0$. The red horizontal shallow circle with arrows on it shows the direction of the precession of $\vec{J}$ around $\vec{B}_0$.

Non-mathematical explanation of the Ramsey method

Here I attempt to elucidate the Ramsey method, devoid of mathematical treatments [82, 83]. Consider an electron with a spin angular momentum, denoted as $\vec{J}$. When this electron is placed within an external magnetic field, $\vec{B}_0$ (upwards in here), $\vec{J}$ initiates a counter-clockwise rotation around the magnetic field at an angular frequency ω_0, a phenomenon known as Larmor precession (see Fig. 5.1). Now, envision a secondary magnetic field, B_1, oriented perpendicular to B_0 and rotating about it at an angular frequency of ω (refer to Fig. 5.2).

Visualizing the motion of $\vec{J}$ under the influence of both $\vec{B}_0$ and $\vec{B}_1$ can be challenging. However, by adopting a rotating frame, the motion is simplified [84]. Imagine a coordinate system rotating around the $\hat{z}$ axis in the same direction and with the same angular frequency as $\vec{B}_1$'s rotation around $\vec{B}_0$. If $\omega = \omega_0$, both $\vec{J}$ and $\vec{B}_1$ appear stationary along a fixed axis. Essentially, it gives the impression of a missing $\vec{B}_0$ and the presence of a static $\vec{B}_1$. Thus, in

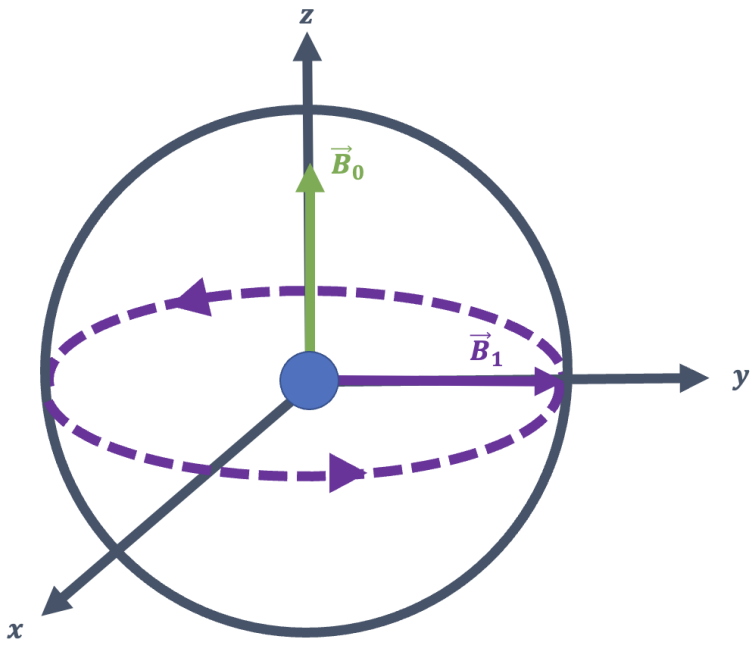

Figure 5.2: Schematic depiction of the rotation of $\vec{B}_1$ about $\vec{B}_0$. The purple arrow shows the direction of $\vec{B}_1$ and the purple horizontal shallow circle with arrows on it shows the direction of $\vec{B}_1$ rotation around $\vec{B}_0$ with angular frequency ω.

this rotating frame, it appears as though $\vec{J}$ is merely precessing around $\vec{B}_1$ (see Fig. 5.3).

Let us now consider a situation where $\vec{B}_1 = 0$. I want to discuss the scenario where $\omega \neq \omega_0$ and we are observing from the rotating frame. Here, we observe $\vec{J}$ precessing around the $\hat{z}$ axis at an angular frequency $\Delta\omega = \omega - \omega_0$, referred to as detuning. Therefore, it appears as if there is a magnetic field in the $\hat{z}$ direction around which $\vec{J}$ is rotating. We also know that the angular frequency of $\vec{J}$'s precession around this magnetic field is influenced by the magnetic field's strength. Thus, the detuning's magnitude determines the strength of the magnetic field that $\vec{J}$ precesses around in the rotating frame. Let us refer to this magnetic field as $\vec{B}_{\Delta\omega}$.

Now, I explain the effect of introducing $\vec{B}_1$. In this scenario, $\vec{J}$ precesses around an axis formed by the sum of $\vec{B}_1$ and $\vec{B}_{\Delta\omega}$. As visualized in Fig. 5.4, the length of $\vec{B}_{\Delta\omega}$ is contingent on the power of the field; a larger detuning corresponds to a longer vector. It is evident that when $|\Delta\omega|$ increases significantly, the precession axis aligns with the $\hat{z}$ axis, negating any rotation of $\vec{J}$ around $\vec{B}_1$. Conversely, in the absence of detuning, the precession axis aligns

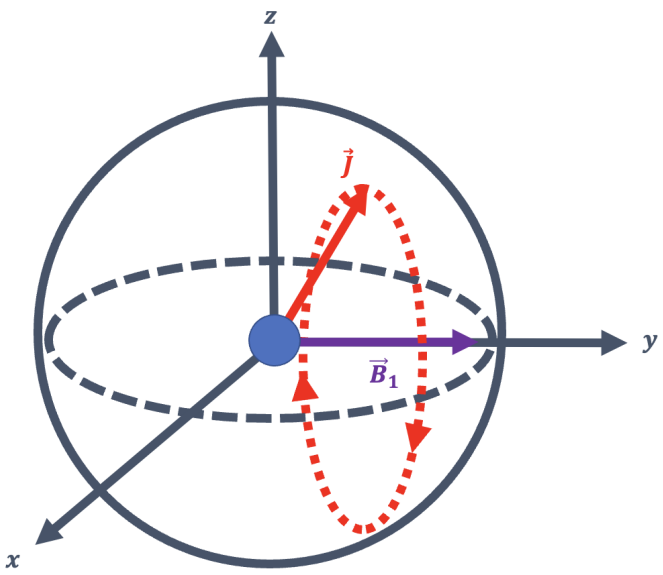

Figure 5.3: Schematic illustration of $\vec{J}$ motion in a coordinate system that rotates around the $\hat{z}$ axis with angular frequency ω_0. The red dotted line with arrows on it indicates the precession of $\vec{J}$ around $\vec{B}_1$.

with $\vec{B}_1$, causing $\vec{J}$ to revolve around $\vec{B}_1$ similar to what is depicted in Fig. 5.3.

Now we are ready to explain the Ramsey method [82, 83, 84]. To simplify, the method is outlined in the rotating frame. The process commences with $\vec{J}$ parallel to the $\hat{z}$ axis and $\vec{B}_1$ being applied briefly, for a time τ, in the $\hat{y}$ direction. Following this, the amplitude of $\vec{B}_1$ is reduced to zero for a relatively extensive period, T_{R} (considerably longer than τ), which corresponds to the Ramsey time in Eq. (2.3). Subsequently, $\vec{B}_1$ is reapplied for a duration of τ. In the cesium beam clock (Fig. 2.2), $\vec{B}_1$ is applied within the arms of the U-shaped cavity, while between the arms, it is deactivated. In the cesium fountain (Fig. 2.4), $\vec{B}_1$ is present only during the short interval when atoms traverse the microwave cavity.

Figure 5.5 illustrates the evolution of $\vec{J}$ during the Ramsey method. By choosing an appropriate magnitude for $\vec{B}_1$, it is feasible to achieve $\theta = \pi/2$ and $\phi = 0$ at the conclusion of the initial application of $\vec{B}_1$. In the area without $\vec{B}_1$, $\vec{J}$ revolves around $\vec{B}_{\Delta\omega}$ at an angular frequency $\Delta\omega$. Once the particle re-enters the region where $\vec{B}_1$ is reapplied, a torque is once again introduced, influencing θ.

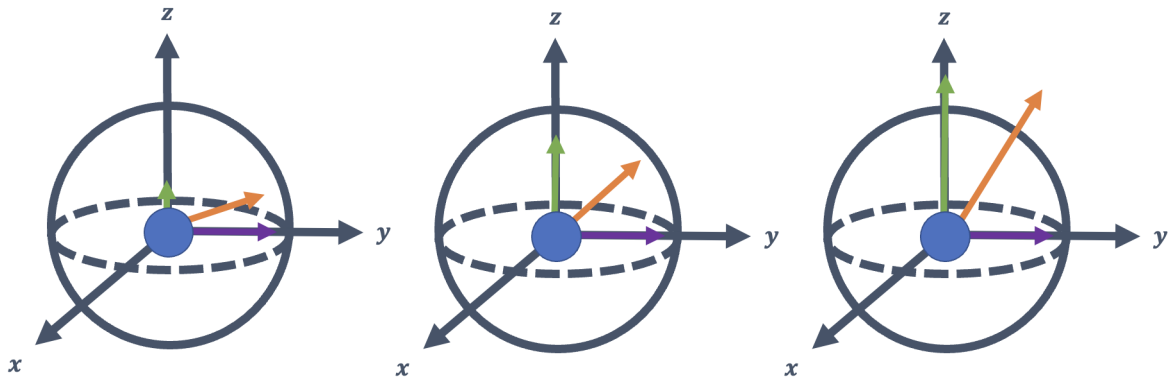

Figure 5.4: Schematic depiction of $\vec{J}$ precession axis in the rotating frame when we have detuning. The orange arrow shows the precession axis and is the addition of $\vec{B}_{\Delta\omega}$ and $\vec{B}_1$ shown by green and purple arrows, respectively.

In the instance where $\Delta\omega = 0$, no precession transpires between the two instances of $\vec{B}_1$ application. As a result, if the magnitude of $\vec{B}_1$ and the duration of its second application mirror those of its first application, the impact of $\vec{B}_1$ remains consistent, resulting in $\vec{J}$ aligning along the $-\hat{z}$ axis. This corresponds to a complete reversal of $\vec{J}$'s direction. However, when $\Delta\omega \neq 0$, $\vec{J}$ precesses around $\vec{B}_{\Delta\omega}$ in the region devoid of $\vec{B}_1$. Assuming that $\Delta\omega T_{\mathrm{R}} = \pi$, $\vec{J}$ would align in the $-\hat{x}$ direction at the moment the second $\vec{B}_1$ is applied. In this scenario, the second $\vec{B}_1$ restores $\vec{J}$ to its original orientation, thereby preventing a transition.

Mathematical treatment of the Ramsey method

Having grasped the conceptual foundation of the Ramsey method, we can now proceed to its mathematical treatment, making use of the Bloch sphere [85]. This graphical tool, depicted in Fig. (5.6), aids us in comprehending the quantum state corresponding to each $\vec{J}$ configuration discussed earlier. The depicted quantum state $|\psi\rangle$ is mathematically expressed as

$$|\psi\rangle = \cos\frac{\theta}{2}|0\rangle + \mathrm{e}^{\mathrm{i}\phi}\sin\frac{\theta}{2}|1\rangle\,. \tag{5.1}$$

Having mapped the abstract quantum states onto the intuitive representation of the Bloch sphere, let us delve into the sequential transformation of the quantum state in the context

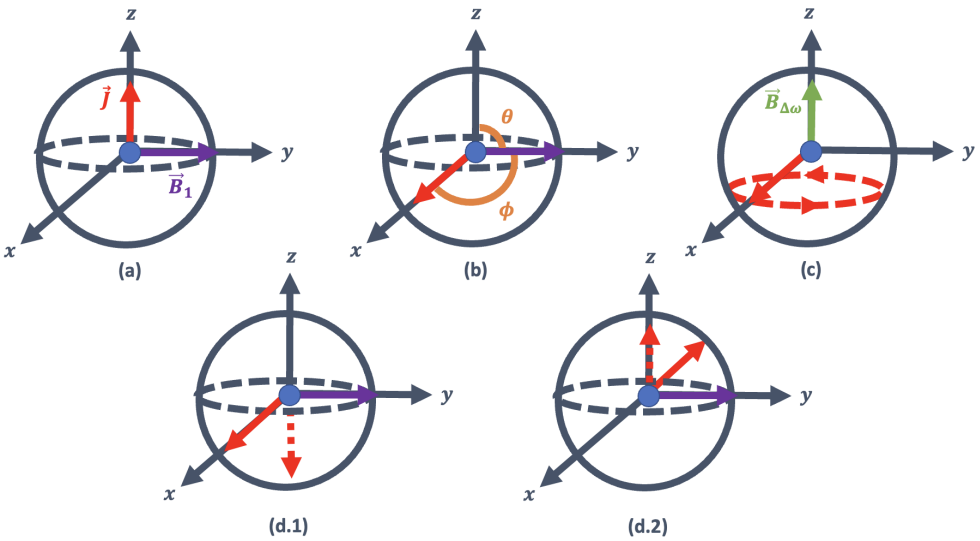

Figure 5.5: Schematic depiction of the evolution of $\vec{J}$ in the Ramsey method. (a) shows the initial condition. (b) shows the next step where $\vec{J}$ precesses about $\vec{B}_1$ and end up in the $\hat{x}$ direction. (c) shows the precession of $\vec{J}$ about $\vec{B}_{\Delta\omega}$ in the absence of $\vec{B}_1$. Both (d.1) and (d.2) show the last step when $\vec{B}_1$ is applied again. (d.1) shows the transfer of $\vec{J}$ form the $\hat{x}$ direction to $-\hat{z}$ direction. This corresponds to $\Delta\omega = 0$. (d.2) corresponds to $\Delta\omega \neq 0$ and shows the motion of $\vec{J}$ from $-\hat{x}$ direction to $\hat{z}$ direction.

of the Ramsey method.

In the rotating frame version of the Ramsey method, the initial orientation of $\vec{J}$ is along the $\hat{z}$ axis, which corresponds to $\theta = 0$. Hence, we have

$$|\psi_1\rangle = |0\rangle\,. \tag{5.2}$$

Subsequently, $\vec{J}$ aligns with the $\hat{x}$ direction, implying that $\theta = \pi/2$ and $\phi = 0$. Thus, we find

$$|\psi_2\rangle = \frac{1}{\sqrt{2}}\left(|0\rangle + |1\rangle\right). \tag{5.3}$$

Next, $\vec{J}$ undergoes precession around the $\hat{z}$ axis, forming an angle $\phi = \Delta\omega T_{\mathrm{R}}$ with the $\hat{x}$ axis. This results in

$$|\psi_3\rangle = \frac{1}{\sqrt{2}}\left(|0\rangle + \mathrm{e}^{\mathrm{i}\phi}\,|1\rangle\right). \tag{5.4}$$

The last step involves a second application of $\vec{B}_1$, causing $\vec{J}$ to rotate around the $\hat{y}$ axis by

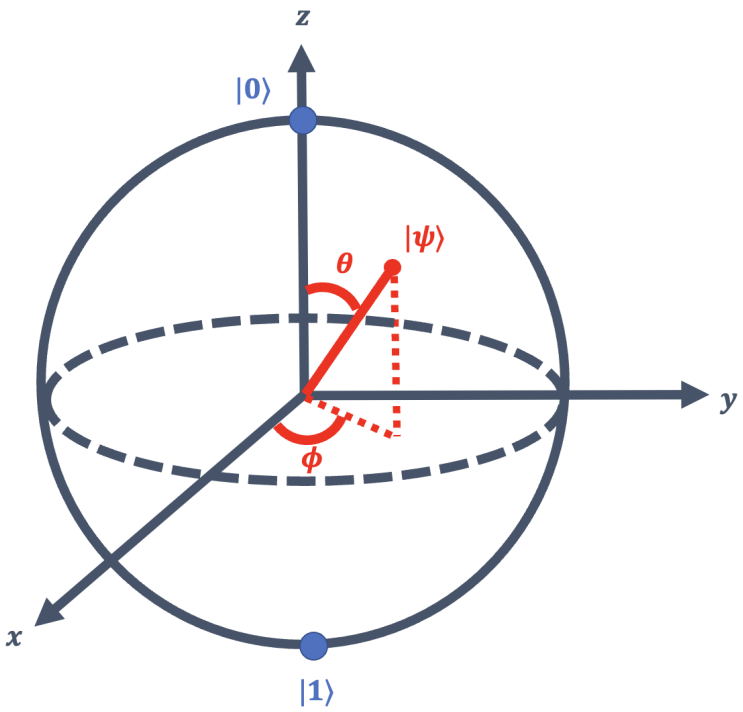

Figure 5.6: Schematic depiction of the Bloch sphere.

an angle $\theta = \pi/2$. The corresponding rotation matrix around the $\hat{y}$ axis is given by [85]

$$R_y\left(\frac{\pi}{2}\right) = \frac{1}{\sqrt{2}}\begin{pmatrix} 1 & -1 \\ 1 & 1 \end{pmatrix}. \tag{5.5}$$

Defining the quantum states as follows

$$|0\rangle := \begin{pmatrix} 1 \\ 0 \end{pmatrix}, \; |1\rangle := \begin{pmatrix} 0 \\ 1 \end{pmatrix}. \tag{5.6}$$

allows us to express the final state as

$$|\psi_4\rangle = R_y\left(\frac{\pi}{2}\right)|\psi_3\rangle = \mathrm{e}^{\mathrm{i}\frac{\phi}{2}}\left(-\mathrm{i}\sin\frac{\phi}{2}|0\rangle + \cos\frac{\phi}{2}|1\rangle\right). \tag{5.7}$$

The final state of $\vec{J}$ after a single Ramsey cycle is given by Eq. (5.7). For zero detuning, i.e., when $\phi = 0$, we find that $|\psi_4\rangle = |1\rangle$, implying a complete transition from $|0\rangle \to |1\rangle$.

Conversely, a detuning such that $\phi = \pi$ yields $|\psi_4\rangle = |0\rangle$, corresponding to no transition.

The probability P of ending up in state $|1\rangle$ is [86]

$$P = |\langle\psi_4|1\rangle|^2 = \frac{1}{2}(1 + \cos\phi) = \frac{1}{2}[1 + \cos(\Delta\omega T_{\mathrm{R}})]. \tag{5.8}$$

The uncertainty of P, denoted by $\sigma_P = P(1-P)$, which has been meticulously calculated in [86]. Therefore, we can safely omit the proof here due to its straightforward explanation in the reference. Consider N independent and identically distributed (IID) electrons subjected to the Ramsey method simultaneously.

The uncertainty σ_P under this scenario is

$$\sigma_P = \sqrt{\frac{P(1-P)}{N}}. \tag{5.9}$$

Applying the propagation of error [87], we can derive the uncertainty in the estimated value of $\Delta\omega$ as [86, 25]

$$\sigma_{\Delta\omega} = \frac{\sigma_P}{|\mathrm{d}P/\mathrm{d}\Delta\omega|} = \frac{1}{T_{\mathrm{R}}\sqrt{N}}. \tag{5.10}$$

The term $\sqrt{N}$ from Eq. (2.3) now makes sense.

However, we observe that while the linewidth is inversely proportional to T_{R}, the instability in Eq. (2.3) scales as $\frac{1}{\sqrt{T_{\mathrm{R}}}}$. To reconcile this, we note that a more accurate version of Eq. (2.3) is [88]

$$\sigma = \frac{\sqrt{T_{\mathrm{R}} + T_d}}{2\pi\nu_0 T_{\mathrm{R}}\sqrt{N}}, \tag{5.11}$$

where T_d is the dead time between Ramsey cycles, primarily arising from the atom preparation and detection periods [89]. In the limit of $T_d \ll T_{\mathrm{R}}$, Eq. (5.11) reverts to Eq. (2.3), demonstrating the origin of the $\frac{1}{\sqrt{T_{\mathrm{R}}}}$ term in Eq. (2.3).

The $\frac{1}{\sqrt{N}}$ scaling (5.10) is a direct consequence of the so called "quantum projection noise" [90]. To understand what quantum projection noise is, we can consider a simple example. Imagine a two-level system in a superposition state $|\psi\rangle = c_a|a\rangle + c_b|b\rangle$. The

outcome of a measurement on $|\psi\rangle$ is deterministic if either c_a or c_b is zero; otherwise, the outcome is unpredictable. This nondeterminism persists irrespective of the precision with which the state is prepared, highlighting an intrinsic aspect of quantum mechanics. This kind of fluctuation in measurement is termed quantum projection noise.

5.2 Quantum-enhanced atomic clocks

An atomic clock whose stability is limited by quantum projection noise [90] and whose atomic transition is driven using Ramsey's method of separated fields with Ramsey time T_{R} has an Allan deviation [52]

$$\sigma_y(\tau) = \frac{1}{2\pi\nu_0\sqrt{NT_{\mathrm{R}}}}\frac{1}{\sqrt{\tau}}. \tag{5.12}$$

By comparing Eq. (5.12) with Eq. (4.27) we write

$$\sigma = \frac{1}{2\pi\nu_0\sqrt{NT_{\mathrm{R}}}} \tag{5.13}$$

as the diffusion coefficient of a free-running clock. The discussion in this section is focused entirely on free-running clocks as this is the focus of the literature on quantum-enhanced atomic clocks. The $1/\sqrt{N}$ scaling (5.12) is commonly referred to as the SQL [23].

Any scaling better than $1/\sqrt{N}$ is an indication that quantum resources such as entanglement of the energy states of the n atoms are used. In other words, if we write

$$\sigma \propto N^{-\delta}, \tag{5.14}$$

then $1/2 < \delta \leq 1$ is an indication of utilizing quantum resources and surpassing of SQL. The potential of theoretically surpassing the SQL has been proposed for quite some time [24]. The idea is as follows: consider N atoms similar to those discussed in the preceding section. Instead of initiating each atom in $|0\rangle$, we begin with a quantum entangled state such as the

Greenberger–Horne–Zeilinger (GHZ) state

$$|\psi_{\mathrm{e}}\rangle = \frac{1}{\sqrt{2}} \left(|00\ldots0\rangle + |11\ldots1\rangle \right), \tag{5.15}$$

where the subscript 'e' denotes entanglement to avoid confusion with $|\psi\rangle$ from the earlier section.

In this scenario, after the third step of the Ramsey method, we acquire [25]

$$|\psi_{\mathrm{e}}\rangle = \frac{1}{\sqrt{2}} \left(|00\ldots0\rangle + \mathrm{e}^{\mathrm{i}N\phi} |11\ldots1\rangle \right). \tag{5.16}$$

Comparing Eqs. (5.16) and (5.4), we observe that ϕ is scaled by N in the entangled state. The probability P_{e} of finding the system in state $|1\rangle$ is

$$P_{\mathrm{e}} = \frac{1}{2} \left[1 + \cos\left(N \Delta\omega_{\mathrm{e}} T_{\mathrm{R}} \right) \right]. \tag{5.17}$$

Hence, the uncertainty in the estimated value of $\Delta\omega_{\mathrm{e}}$ becomes

$$\sigma_{\Delta\omega_{\mathrm{e}}} = \frac{1}{N T_{\mathrm{R}}}. \tag{5.18}$$

Comparing Eqs. (5.15) and (5.10), it is clear that the uncertainty is reduced by a factor of $\sqrt{N}$ in the entangled state compared to the non-entangled state. The potential for improvement in atomic clock stability by a factor of $\sqrt{N}$ is the core quantum advantage for these clocks. The $1/N$ scaling in atomic clock stability, known as the Heisenberg limit, is posited as the fundamental limitation for atomic clock stability that cannot be surpassed [24].

Now, consider a network of M atomic clocks. Suppose all these atomic clocks are founded on the same atomic element, say, cesium, and that each atomic clock contains N atoms. One could entangle all the MN atoms in the network using the quantum teleportation technique, thereby establishing a quantum network of atomic clocks [91]. By implementing

an appropriate protocol, the stability of all the atomic clocks in this network is enhanced by a factor of $\sqrt{MN}$.

5.3 Noisy Quantum-enhanced atomic clocks

I now discuss the constraints surrounding the use of entangled states for exceeding the standard quantum limit. Huelga et al. [25] illustrated that the adoption of maximally entangled states, such as GHZ state, does not enhance the stability of atomic clocks when faced with Markovian dephasing, a typical source of decoherence in atoms. This occurs because maximally entangled states undergo decoherence at a rate that is N times quicker than non-entangled atoms. Hence, to optimize performance, T_{R} has to be decreased by a factor of N when a maximally entangled state is used. Consequently, the advantages of using maximally entangled states are counterbalanced by the reduction in T_{R} [92], suggesting that they do not enhance the stability of atomic clocks [93].

Given that maximally entangled states provide no benefit, it prompts the question of whether non-maximally entangled states could provide any advantage. Huelga et al. [25] demonstrated that a partially entangled state with high symmetry improves the stability in the presence of Markovian dephasing. However, the extent and manner in which partially entangled states enhance atomic clock stability as $N \to \infty$ remained unclear.

This question was resolved by Escher et al. [26] who showed that regardless of the initial state or the measurement approach, the most enhancement achievable in the presence of Markovian dephasing is by a factor of $\sqrt{\mathrm{e}}$, which does not beat the standard quantum limit. This conclusion holds true even with small dephasing rates if N is sufficiently large. It implies that surpassing the standard quantum limit in atomic clock stability via quantum strategies is unlikely. This conclusion has been extended to other noise models including depolarization, spontaneous emission, and photon loss [27].

These theoretical findings have been verified through experimental means. For exam-

ple, Leroux et al. [31] demonstrated a fully functional quantum-clock with $T_{\mathrm{R}} = 200\mu$s and N on the order of 10^4, illustrating that T_{R} in quantum clocks is shorter than conventional atomic clocks (where $T_{\mathrm{R}} = 1$s) by a factor of 10^4, thereby validating the claim that quantum-enhanced atomic clocks provide no advantage when decoherence is present. Another experimental validation comes from Ref. [32] that demonstrated a quantum-clock with $T_{\mathrm{R}} = 10\mu$s and $N = 10^5$.

Stability enhancement by a factor of $N^{1/4}$ and $N^{1/3}$ might be possible for non-Markovian noise [28, 29] or noise perpendicular to the signal [30], respectively. However, the appropriate Ramsey time T_{R} (5.12) tends to zero for large N in the aforementioned cases: $T_{\mathrm{R}} \in O(N^{-1/2})$ for non-Markovian noise, and $T_{\mathrm{R}} \in O(N^{-1/3})$ for transversal noise. These reduction in T_{R} cancel out the enhancement in N and therefore, $\sigma_y(\tau)$ is not enhanced.

Now we consider the possibility of whether these limitations due to decoherence can be mitigated through the methods of quantum error correction. Quantum error correction mitigates decoherence and restores the Heisenberg limit if the Hamiltonian does not lie in the span of Lindblad operators, a condition known as Hamiltonian-not-in-the-Lindblad-span (HNLS) [34]. Otherwise, the improvement is just a constant factor, even with the use of quantum error correction [35, 36, 34]. Unfortunately, the dephasing noise that dominates atomic clock performance [25, 37] is described by a Lindblad operator, and the Hamiltonian is trivially in the span of that operator. Therefore, atomic clock scaling limitation cannot be mitigated by quantum error correction.

Chapter 6

Approach

In this section, we present our approach to quantify asynchronization between different local representations of UTC reliably. We begin in §6.1 by discussing our model of clocks incorporating $x(t)$, which quantifies the limits to synchronisation of clock networks. Next, we describe our model of clocks mathematically in §6.2. Finally, in §6.3, we describe how we solve the mathematical expressions introduced in §6.2.

6.1 Model

In this section, we introduce our "ballistic clock" model. For intuitive reasons, we employ the analogy of a curling stone sliding on frictionless ice as depicted in Fig. 6.1. Curling is a sport involving curlers (players) sliding stones on an ice rink towards a target with the speed of the stones controlled by sweeping the ice, which provides an excellent picture for our ballistic-clock model, which we introduce for an intuitive understanding of the mathematics in Chapter 4. Finally, we extend our model to the quantum case.

In our picture, an observer can tell how much time has passed simply by looking at where the stone, moving at a known constant velocity, is on the ice rink. We then delve into the imperfection of the moving curling stone by analysing environmental effects—i.e., noise—on the model. Our noise model allows for random scattering events only along the

one-dimensional path of motion for the stone. Then we discuss a constrained ballistic clock. Next, we expand this model to a network of coupled ballistic clocks. Finally, we relate our network of coupled ballistic clocks to the UTC network.

Our model for a clock is founded on the concept of a ballistic-clock using the analogy of a moving curling stone. We explain our model and justify why this moving stone on frictionless ice is a proper clock. In Fig. 6.1, we depict a curling stone moving frictionlessly and at a constant velocity along a one-dimensional path ice marked with equally spaced intervals. Just as a pendulum swings back and forth, which is known onomatopœically as "tick-tock", we regard the stone motion as being a 'tick' or a 'tock' as it moves through alternating intervals. Thus, one "tick-tock" time unit, corresponding to one clock oscillation, occurs when the stone crosses two intervals.

Time is determined by counting these oscillations, i.e., the number of "tick-tock" events. The stone's velocity establishes the frequency of these "tick-tock" oscillations. In the sport of curling, this velocity can be modified by a sweeper who uses a broom to change the friction of the ice and thereby control the velocity. This model of a clock correctly keeps time by counting, just as typical physical clocks such as pendulum or atomic clocks, do.

Incorporating environmental noise into our ballistic-clock model, we examine the effect of this noise on the stone's velocity and position, analogous to a clock's frequency and phase. We focus solely on the impact of stochastic noise on clock frequency, not deterministic effects such as drift, which would cause irrelevent effects like frequency increasing or decreasing. Consequently, we disregard deterministic forces causing deceleration of the curling stone's motion, such as friction. Our noise model, based on one-dimensional random scattering of the stone along the direction of motion and no friction, captures the essence of frequency fluctuations of a clock. Inclusion of noise on the velocity of the stone causes its position to diffuse, as shown in Fig. 6.1(b).

We now turn our attention to a constrained ballistic clock. Imagine a sweeper with a brush that is able to modify the surface of the ice rink to control the velocity of a ballistic

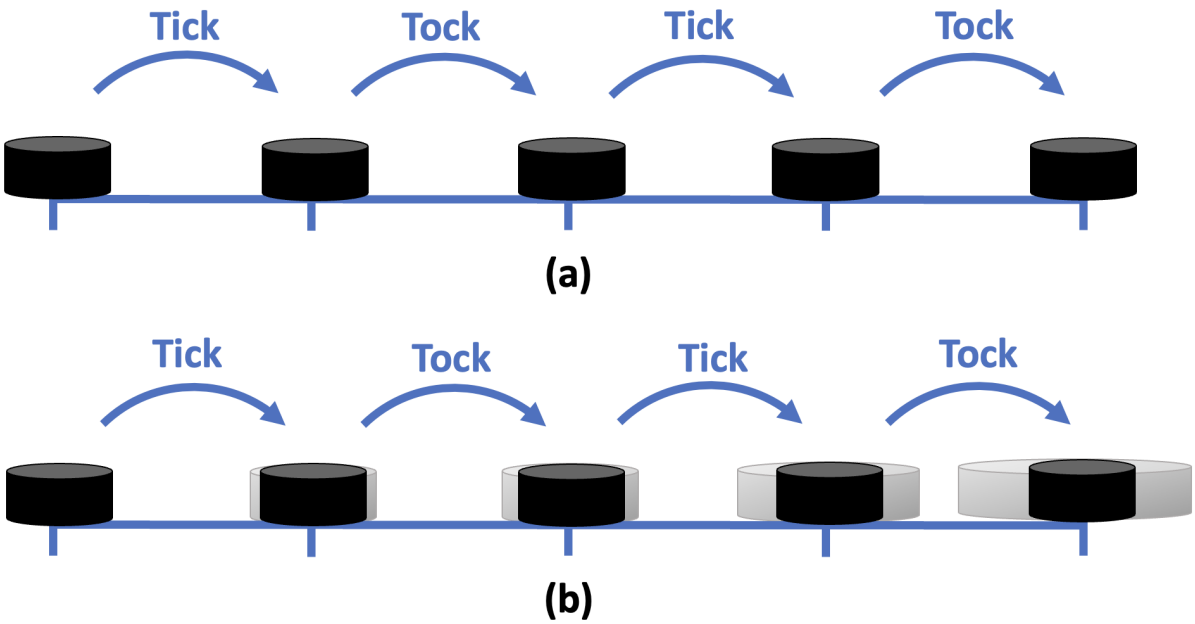

Figure 6.1: Clock described as a curling stone moving in one dimension on ice divided into equal intervals by vertical blue lines. The ice is frictionless but can invoke random scattering of the stone's velocity along the direction of motion. We see (a) the ideal noiseless case and (b) the noisy case. The arrows show the stone's movement from one interval to the next, corresponding to the tick-tock of a clock. The shadows around the stone in (b) expand as the stone moves forward, illustrates diffusion of the stone's position.

clock. Moreover, imagine two curling stones beside each other with one being ideal and the other one being noisy, which is monitored and controlled by a sweeper. The noisy ballistic clock is considered constrained if the sweeper forces the position of the noisy clock back towards the ideal with modifying its velocity. We see that this is similar to a constrained atomic clock which is steered in frequency so that its time is forced towards μ with κ (4.24).

Expanding upon the concept of a constrained ballistic clock, let us consider a network of these clocks. Imagine multiple noisy ballistic clocks on an ice rink, each with the same initial position and velocity, and each monitored by a sweeper. Moreover, imagine that there is a master that is able to calculate and broadcast the average of the positions of all the ballistic clocks in real-time. The task of each sweeper is to adjust their ballistic-clock velocity by sweeping the ice, intending to align the position of their ballistic clock with the average position that is announced by the master. We assume that κ is identical for all the ballistic clocks.

Drawing parallels to the UTC network, each ballistic clock in our coupled network represents a UTC(k), with the average representing UTC itself. Similar to how each UTC(k) is steered in frequency to maintain synchronisation to UTC, each ballistic clock is steered in velocity so that its position is aligned to the average. The master plays the role of BIPM with the distinction that BIPM announces the average with a time delay of about two weeks.

In extending our ballistic-clock model to the quantum domain, we employ a Wigner function approach [94] to represent the state of our system. The Wigner function, a quasiprobability distribution, is particularly suited for this model as it provides a complete description of the quantum state in phase space, encapsulating both position and momentum. We begin with two free-running ballistic clocks and denote by $Q(t)$ their relative position with respect to each other. We initialize their state with a joint probability distribution $P(Q_0, P_0)$, where Q_0 and P_0 are the initial relative position and momentum, respectively. The evolution of this system is governed by a SDE that preserve the Gaussian nature of the initial distribution. The Gaussian-preserving evolution allows us to treat the Wigner function as a

probability distribution for the purposes of our model.

We analyze two scenarios: independent and entangled ballistic-clocks. In the independent scenario, the uncertainty in both the initial relative position and momentum conforms to the vacuum uncertainty. However, for the entangled scenario, we squeeze the uncertainty in the initial relative position, with the squeezing parameter r representing the degree of entanglement [95]. The choice of the uncertainties in our model is designed to match those of the Wigner function, ensuring that our representation accurately reflects the quantum mechanical nature of the system.

6.2 Mathematics

In this subsection, we describe our ballistic-clock model mathematically. We begin by deriving the SDE for the relative position of a noisy constrained ballistic clock with respect to an ideal one. Next we derive the SDE for the case of a coupled network of ballistic clocks. We then explain how to calculate the covariance matrix for the vector $\boldsymbol{q}(t)$, where each element $q_i(t)$ represents the relative position of the i^{th} ballistic clock with respect to an ideal one. Finally, we discuss how we extend our model mathematically to the quantum case.

To derive the SDE for $q(t)$, we assume that the relative velocity $\dot{q}(t)$ experiences white noise, which is analogous to atomic-clock white noise on $y(t)$ (4.9). Similar to how white noise on $y(t)$ imposes a Wiener process on $x(t)$, white noise on $\dot{q}(t)$ imposes a Wiener process on $q(t)$. In addition, assuming that the ballistic clock is constrained to a time-dependent value $\mu(t)$,

$$\mathrm{d}q(t) = -\kappa\left[q(t) - \mu(t)\right]\mathrm{d}t + \sigma \mathrm{d}W(t). \tag{6.1}$$

We see that Eq. (6.1) is analogous to Eq. (4.24) with the distinction that μ is time-dependent.

Now we derive the SDE for a network of coupled ballistic clocks. From our coupled-

network description discussed in §6.1, we replace

$$\mu(t) \mapsto \bar{q}(t) := \frac{1}{N}\sum_{i=1}^{N} q_i(t). \tag{6.2}$$

Furthermore, κ is the same for all of the ballistic clocks. Therefore, the SDE for a network of coupled ballistic clocks is

$$\mathrm{d}\boldsymbol{q}(t) = -\kappa\left[\boldsymbol{q}(t) - \bar{q}(t)\mathbf{1}\right]\mathrm{d}t + \sigma\mathrm{d}\boldsymbol{W}(t), \tag{6.3}$$

where **bold** font denotes vectors and $\mathbf{1}$ denotes the vector of all ones.

To calculate the covariance matrix for $\boldsymbol{q}(t)$, we reformulate Eq. (6.3) and demonstrate that coupling each clock to the average is equivalent to coupling each clock to the rest (global coupling). Then we diagonalise Eq. (6.3) and solve. Finally, we derive the covariance matrix

$$\mathrm{cov}\left[\boldsymbol{q}(t)\right] := \left\langle \boldsymbol{q}(t)\boldsymbol{q}^{\dagger}(t)\right\rangle - \left\langle \boldsymbol{q}(t)\right\rangle \left\langle \boldsymbol{q}^{\dagger}(t)\right\rangle \tag{6.4}$$

by using the solution to the diagonalised form of Eq. (6.3).

To extend the model to the quantum case, we start from a joint Gaussian probability distribution in relative position and momentum

$$P(Q_0, P_0) = \frac{1}{2\pi\sigma_{Q_0}\sigma_{P_0}}\exp\left\{-\frac{1}{2}\left(\frac{Q_0^2}{\sigma_{Q_0}^2} + \frac{P_0^2}{\sigma_{P_0}^2}\right)\right\}. \tag{6.5}$$

Our goal now is to see how this joint distribution evolves under

$$\mathrm{d}Q(t) = \frac{P_0}{m}\mathrm{d}t + \sigma\mathrm{d}W(t). \tag{6.6}$$

We remark that $W(t)$ incorporated in the SDE, inherently possesses a normal distribution (4.19). Given that both Q_0 and P_0 are normally distributed and considering the linear nature of the SDE, the evolution is Gaussian-preserving.

Gaussian-preservation arises because a linear combination of normally distributed random variables results in another normally distributed variable. For the independent case, we assume [96]

$$\sigma_{Q_0} = \sqrt{\frac{\hbar}{2m\omega}},\ \sigma_{P_0} = \sqrt{\frac{\hbar m\omega}{2}}, \tag{6.7}$$

and for the entangled case, we replace [94]

$$\sigma_{Q_0} \to \sigma_{Q_0}\mathrm{e}^{-r},\ \sigma_{P_0} \to \sigma_{P_0}\mathrm{e}^{r}. \tag{6.8}$$

In the limit that r goes to infinity

$$\lim_{r\to\infty} \sigma_{Q_0}\mathrm{e}^{-r} = 0, \tag{6.9}$$

which means that the position of clocks are perfectly correlated, similar to an EPR-like state [95].

6.3 Methods

In this subsection, we present our methods for calculating the covariance matrix (6.4). First, we discuss our method for showing that coupling each clock to the average (6.3) is equivalent to global coupling. Next, we discuss our method for diagonalising Eq. (6.3) and how to solve. Then we discuss our method for deriving $\mathrm{cov}[\boldsymbol{q}(t)]$ based on the solution to the diagonalised form of Eq. (6.3). Finally, we elaborate on our method for deriving the evolved joint distribution (6.5).

To show the global coupling, we first subtract $\boldsymbol{q}(t)$ from $\bar{q}(t)\mathbf{1}$. Then we rewrite this result in terms of the the product of a matrix C with $\boldsymbol{q}(t)$, where $C\boldsymbol{q}(t)$ exposes the global coupling through each of its entries being a linear combination of $\boldsymbol{q}(t)$ with different weightings. As all coupling are the same in our model, C is a circulant matrix.

We are now ready to diagonalise and solve the equations. First, we calculate the spectral

decomposition of C. The spectral decomposition is obtained by conjugating the spectrum of spec C by the discrete Fourier transform matrix D [97], i.e.,

$$C = D \operatorname{spec} C D^{\dagger} \tag{6.10}$$

for

$$D := \frac{1}{\sqrt{N}} \begin{pmatrix} 1 & 1 & 1 & \dots & 1 \\ 1 & z_N & z_N^2 & \dots & z_N^{N-1} \\ 1 & z_N^2 & z_N^4 & \dots & z_N^{2(N-1)} \\ \vdots & \vdots & \vdots & & \vdots \\ 1 & z_N^{N-1} & z_N^{2(N-1)} & \dots & z_N^{(N-1)^2} \end{pmatrix}, \tag{6.11}$$

with $z_N := \mathrm{e}^{2\pi \mathrm{i}/N}$, i.e., the N^{th} root of one.

Then we perform a basis transformation $D\boldsymbol{q}(t) =: \boldsymbol{q}'(t)$. Thus,

$$D\boldsymbol{W} =: \boldsymbol{W}'(t), \tag{6.12}$$

which effectively diagonalise the equations. Finally, we determine the mean and variance in this new basis by mapping known solutions of the OU process (4.25).

To derive the covariance matrix (6.4), we write Eq. (6.4) in terms of $\boldsymbol{q}'(t)$. Then as the components of $\boldsymbol{q}'(t)$ are mutually independent, we rewrite $\operatorname{cov}[\boldsymbol{q}(t)]$ in terms of the diagonal elements of $\operatorname{cov}[\boldsymbol{q}'(t)]$, which are the variances $\sigma_i'^2$ for the i^{th} component. Finally, we perform the inverse trasnformation to obtain $\operatorname{cov}[\boldsymbol{q}(t)]$.

Finally, we elaborate on our method to derive the evolved joint distribution of $P(Q_0, P_0)$. First, we use the Itô interpretation, and rewrite Eq. (6.6) as a stochastic integral equation with integration time τ [98]. Then we note that $P(Q_0, P_0)$ (6.5) can be written as the product of two Gaussian distributions $P(Q_0)$ and $P(P_0)$. Finally, we simply derive the evolved joint distribution $P(Q; \tau)$ by noting that $Q(\tau)$ has a normal distribution as it is a linear combination of normal distributions.

Chapter 7

Results

In this chapter, we present our main results. First, we derive the SDE that demonstrates global coupling. second, we provide the solutions of the diagonlised equations. Next, we derive the closed form expression for $\mathrm{cov}[\boldsymbol{q}(t)]$. Ultimately, we move on to the quantum case and derive $P(Q;\tau)$.

Now we derive the SDE that demonstrates global coupling by following all the steps described in ¶2 of §6.3, with $\mathbb{1}$ denoting the identity matrix and $\mathbb{J}$ the matrix of all ones. Then

$$\mathrm{d}\boldsymbol{q}(t) = -C\boldsymbol{q}(t)\mathrm{d}t + \sigma\mathrm{d}\boldsymbol{W}(t), \tag{7.1}$$

where

$$C = \frac{\kappa}{N}\left(N\mathbb{1} - \mathbb{J}\right), \tag{7.2}$$

is the circulant matrix.

To derive and solve the SDE for the diagonalised equations, we follow the steps described in ¶3 and ¶4 of §6.3. Thus, we derive

$$\mathrm{d}\boldsymbol{q}'(t) = -\mathrm{diag}(\boldsymbol{\kappa})\boldsymbol{q}'(t)\mathrm{d}t + \sigma\mathrm{d}\boldsymbol{W}'(t) \tag{7.3}$$

for

$$\boldsymbol{\kappa} = (\kappa_i),\ \kappa_i := \kappa(1 - \delta_{i1}). \tag{7.4}$$

Assuming $\boldsymbol{q}'(0) = \mathbf{0}$, with $\mathbf{0}$ as the vector of all zeros, the solutions to Eq. (7.3) are

$$q_1'(\tau) = \sigma \int_0^\tau \mathrm{d}W_1'(t) \sim \mathcal{N}\left(0, \sigma^2\tau\right) \tag{7.5}$$

for $i = 1$, and

$$\begin{aligned} q_i'(\tau) &= \sigma \int_0^\tau \mathrm{d}W_i'(t)\, \mathrm{e}^{-\kappa(\tau - t)} \\ &\sim \mathcal{N}\left(0, \frac{\sigma^2}{2\kappa}\left(1 - \mathrm{e}^{-2\kappa\tau}\right)\right) \end{aligned} \tag{7.6}$$

for

$$i \in [2, N] := \{2, \ldots, N\}. \tag{7.7}$$

Here $\sim \mathcal{N}$ denotes scaling as a normal distribution (4.19).

To derive $\mathrm{cov}[\boldsymbol{q}(t)]$(6.4), we first produce the results of each step in ¶5 of §6.3. The result of the first step is

$$\mathrm{cov}\left[\boldsymbol{q}(t)\right] = D^\dagger \mathrm{cov}\left[\boldsymbol{q}'(t)\right] D. \tag{7.8}$$

The result of the second step with $\bar{\mathbb{1}}$ as the complement of the identity matrix is

$$\begin{aligned} \mathrm{cov}\left[\boldsymbol{q}(\tau)\right] = \frac{1}{N}\Big\{ &\left[\sigma^2_{q_1'}(\tau) + (N-1)\sigma^2_{q_i'}(\tau)\right] \mathbb{1} \\ &+ \left[\sigma^2_{q_1'}(\tau) - \sigma^2_{q_i'}(\tau)\right] \bar{\mathbb{1}}\Big\}. \end{aligned} \tag{7.9}$$

The result of the third step is

$$\begin{aligned} \mathrm{cov}\left[\boldsymbol{q}(\tau)\right] = \frac{\sigma^2\tau}{N}\Bigg\{ &\left[1 + \frac{N-1}{2\kappa\tau}\left(1 - \mathrm{e}^{-2\kappa\tau}\right)\right] \mathbb{1} \\ &+ \left[1 - \frac{1}{2\kappa\tau}\left(1 - \mathrm{e}^{-2\kappa\tau}\right)\right] \bar{\mathbb{1}}\Bigg\}, \end{aligned} \tag{7.10}$$

which gives us the variance and covariance of the relative position of the noisy ballistic clocks

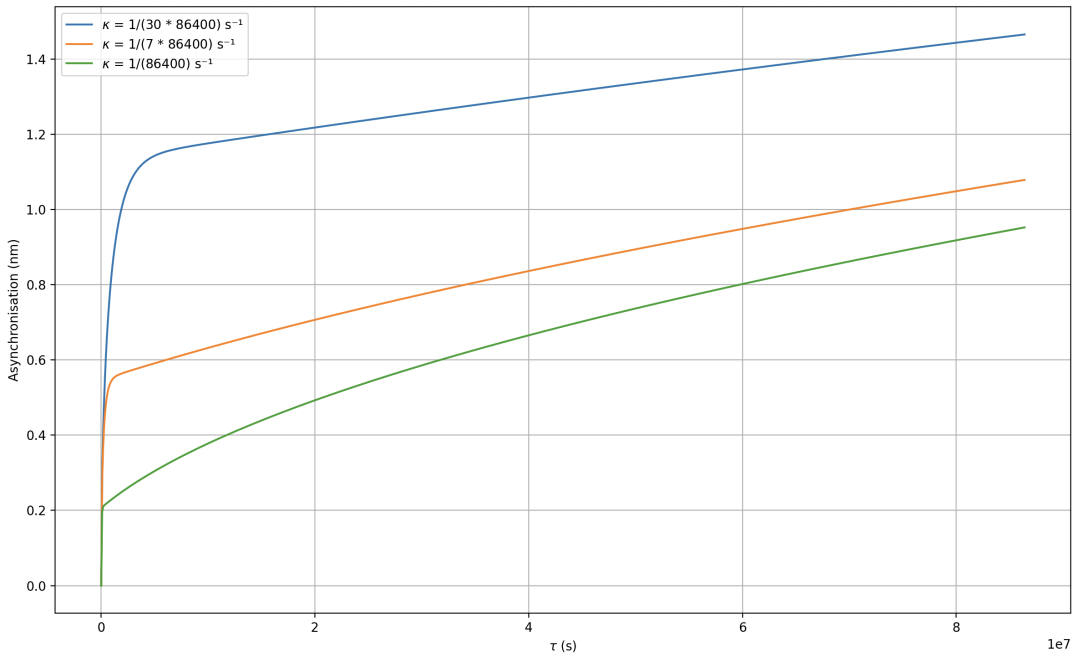

Figure 7.1: Asynchronisation for $\sigma = 10^{-12}\,\mathrm{m}/\sqrt{\mathrm{s}}$ and $N = 100$.

with respect to an ideal one. We show how the diagonal elements of this matrix change with respect to τ for different κ in Fig. 7.1, different N in Fig. 7.2, and different σ in Fig. 7.3. We discuss the figures in Chapter 8.

We now turn our attention to the quantum case. To derive $P(Q;\tau)$, we begin by rewriting Eq. (6.6) as a stochastic integral equation

$$Q(\tau) = Q_0 + \frac{P_0}{m}\tau + \sigma\int_0^\tau \mathrm{d}W(t). \tag{7.11}$$

Then we readily write

$$P(Q;\tau) = \frac{1}{\sigma_Q(\tau)\sqrt{2\pi}}\mathrm{e}^{-\frac{1}{2}\frac{Q^2}{\sigma_Q^2(\tau)}}, \tag{7.12}$$

where

$$\sigma_Q^2(\tau) = \sigma_{Q_0}^2 + \frac{\sigma_{P_0}^2}{m^2}\tau^2 + \sigma^2\tau, \tag{7.13}$$

with σ_{Q_0} and σ_{P_0} satisfying Eqs. (6.7) and (6.8) for the independent and entangled cases, respectively.

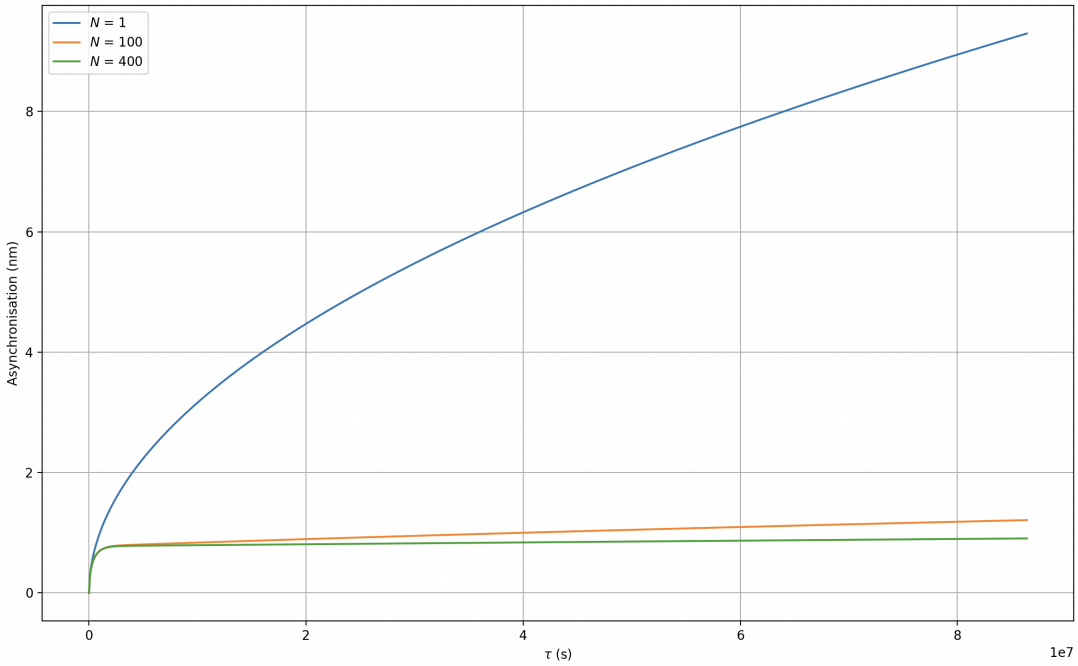

Figure 7.2: Asynchronisation for $\kappa = \frac{1}{14\times86400}\,\mathrm{s}^{-1}$ and $\sigma = 10^{-12}\,\mathrm{m}/\sqrt{\mathrm{s}}$.

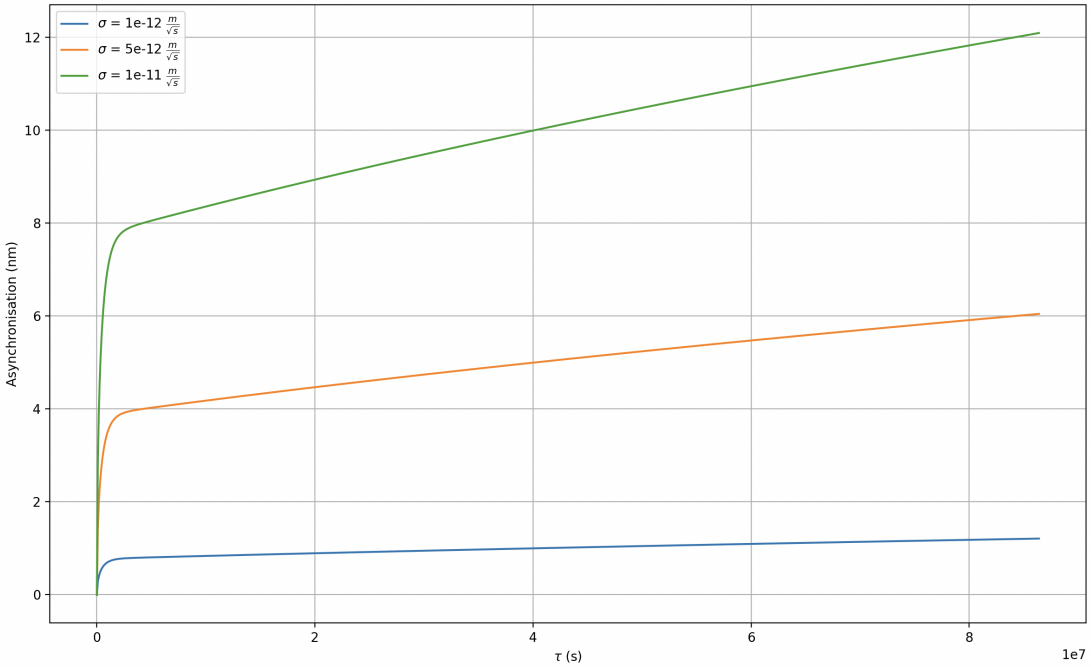

Figure 7.3: Asynchronisation for $\kappa = \frac{1}{14\times86400}\,\mathrm{s}^{-1}$ and $N = 100$.

For the entangled case, $\sigma_Q(\tau)$ is smaller than for the independent case until the time

$$\tau_r = \frac{\mathrm{e}^{-r}}{\omega} \tag{7.14}$$

is reached, where the trivial singularity at $r = 0$ is removed by replacing that point by its equal left and right limits over r. Thus, entanglement ceases to offer any advantage at finite time. Evidently, $\tau_\infty = 0$ meaning that, if two clocks are prepared in an EPR state, entanglement has no advantage compared to the independent-preparation case for any duration of time. At the other limit, $\tau_0 = 1/\omega$ meaning that any vestige of arbitrarily small entanglement is completely lost by τ_0.

Chapter 8

Discussion and conclusion

In this chapter, we discuss our results. We begin by elaborating on the significance of the diagonal elements of Eq. (7.10). Then we elaborate on how on can use the diagonal elements to perform a stability analysis. Next, we elaborate on the significance of the non-diagonal elements of Eq. (7.10). Then, we elaborate further on Eq. (7.14) and conclude the thesis in the end.

The diagonal elements of $\mathrm{cov}\,[\boldsymbol{q}(t)]$ is the variance of $\boldsymbol{q}(t)$, namely, $\sigma^2_{\boldsymbol{q}(t)}$. The square root of this variance quantifies the asynchronisation between each UTC(k) with respect to an ideal time scale such as UTC (ideal in comparison to UTC(k)). When $\kappa\tau \to \infty$, the diagonal elements of Eq. (7.10) reduce to

$$\sigma_{\boldsymbol{q}(t)} = \frac{\sigma}{\sqrt{N}}\sqrt{\tau}, \tag{8.1}$$

which means that the stability of each UTC(k) is enhanced by a factor of $\sqrt{N}$ as opposed to if they were not coupled. The $\sqrt{N}$ enhancement is anticipated because when $\kappa\tau \to \infty$, each UTC(k) is replaced by the average time scale (UTC).

As seen in Fig. 7.1, the higher the κ, the lower the asynchronisation. Therefore, the faster the UTC(k) sites remove their time offset from UTC, the smaller the asynchronisation becomes. However, as discussed in §3.3, if UTC(k) sites want to preserve the short-term

stability of their time scale, they must limit the value of κ. This limitation ensures that the change in frequency is comparable to the inherent frequency fluctuations of their time scale.

Figure 7.2 shows that the higher the number of clocks, the smaller the asynchronisation. Therefore, with more labs joining the UTC network, not only is UTC stability enhanced, but also the asynchronisation of each UTC(k) with respect to UTC. Finally, Fig. 7.3 demonstrates that the smaller the diffusion coefficient, the smaller the asynchronisation. Hence, the asynchronisation of UTC(k) with respect to UTC could be reduced by using more stable clocks. For instance, the asynchronisation is expected to decrease in the future when optical clocks replace microwave clocks.

The non-diagonal elements of Eq. (7.10) demonstrate that different UTC(k) are correlated to each other, which is in contrary to the assumption that different UTC(k) are independent from one another [6]. Therefore, Eq. (7.10) can be used to determine the correlation between different UTC(k). Quantifying the correlation can have applications for calculating the uncertainty of [UTC $-$ UTC(k)], where the correlation is taken to be zero. There are attempts to introduce correlations, but correlations are typically believed to arise only due to noise in the time links [99]. However, our result shows that there are also correlations due to the steering of each UTC(k) towards UTC.

Lastly, we elaborate on Eq. (7.14). Evidently, the time scale until entanglement provides an advantage over independent preparation becomes exponentially smaller with respect to the degree of entanglement. The EPR limit (τ_∞), suggests that if the two clocks are prepared in a highly entangled state, entangled clocks have no advantage over independent ones. This result matches the well-known result that, in the presence of decoherence, atomic-clock performance is not enhanced by using maximally entangled states [25].

To conclude, in our work, we have identified the absence of an existing model that could quantify the asynchronisation between different UTC(k), pointing out the need to construct such a model. We have built upon two established ideas from previous studies: using the OU process to model the performance of a "constrained clock", and treating UTC(k) as being

coupled to UTC via frequency steering adjustments that attempt to keep UTC(k) and UTC synchronised. Using these ideas, we have constructed a model that views the UTC network as a set of coupled OU processes and introduced our model of ballistic-clock as a physical representation. From this model, we have derived an expression that can quantify not only the asynchronisation between different UTC(k), but also their correlation. decoherence is only a constant factor.

We have extended our model of ballistic clock to the quantum case and showed that the advantage of entanglement in improving synchronization diminishes exponentially with the degree of entanglement over time. Our results resonate with a previous study establishing that maximally entangled states do not necessarily enhance clock performance in the presence of decoherence [25]. This finding has profound implications for the development of future quantum timekeeping technologies, suggesting a nuanced approach towards leveraging quantum entanglement for improved precision and stability as the advantage of entanglement can be fragile. This subtlety underlines the importance of strategic entanglement utilization, optimizing the benefits while mitigating the limitations imposed by real-world conditions.

There are various potential paths for further research. First, we assumed that all UTC(k) have identical diffusion coefficient and mean-reversion rate, which is not the case in practice. Therefore, one option is to solve Eq. (6.3) with different σ and κ for each clock. Second, we assumed that UTC(k) is only affected by white frequency noise, but to strengthen the model one could incorporate random walk frequency noise, which dominants the white noise in long averaging times. Third, we assumed that the average of the position of clocks is calculated and broadcast in real-time, which is not the case in reality where there is a time delay. Therefore, another future work should solve Eq. (6.3) with a time delay by replacing $\bar{q}(t)$ with the known average at the nearest time.

Bibliography

[1] H. Margolis, Phys. World **31**, 27 (2018).

[2] M. A. Lombardi, in *Measurement, Instrumentation, and Sensors Handbook*, edited by J. G. Webster and H. Eren (CRC Press, 2014) Chap. 41, 2nd ed.

[3] M. A. Lombardi, IEEE Instrum. Meas. Mag **14**, 45 (2011).

[4] W. J. H. Andrewes, Sci. Am. **287**, 76 (2002).

[5] A. Jones, *Splitting the second: The story of atomic time* (CRC Press, 2000).

[6] G. Panfilo and F. Arias, Metrologia **56**, 042001 (2019).

[7] M. A. Lombardi, in *Encyclopedia of Physical Science and Technology*, edited by R. A. Meyers (Academic Press, Cambridge, 2003) pp. 783–801, 3rd ed.

[8] S. A. Diddams, J. C. Bergquist, S. R. Jefferts, and C. W. Oates, Science **306**, 1318 (2004).

[9] J. Jespersen and J. Fitz-Randolph, *From Sundials to Atomic Clocks*, monograph 155 ed. (US Department of Commerce, Technology Administration, National Institute of Standards and Technology, 1999).

[10] P. Forman, Proceedings of the IEEE **73**, 1181 (1985).

[11] L. Essen and J. V. Parry, Nature **176**, 280 (1955).

[12] M. A. Lombardi, T. P. Heavner, and S. R. Jefferts, NCSLI Measure **2**, 74 (2007).

[13] J. Levine, Eur. Phys. J. H **41**, 1 (2016).

[14] A. Kastler, J. Phys. Rad. **11**, 255 (1950).

[15] D. Sullivan, J. C. Bergquist, J. Bollinger, R. Drullinger, W. Itano, S. Jefferts, W. Lee, D. Meekhof, T. Parker, F. Walls, and D. J. Wineland, J. Res. Natl. Inst. Stand. Technol.. **106**, 47 (2001).

[16] P. Arora, A. Awasthi, V. Bharath, A. Acharya, S. Yadav, A. Agarwal, and A. S. Gupta, Pramana **82**, 173 (2014).

[17] E. F. Arias and G. Petit, Annalen der Physik **531**, 1900068 (2019).

[18] M. A. Lombardi, IEEE Instrumentation & Measurement Magazine **15**, 47 (2012).

[19] P. Arora and A. Sen Gupta, in *Handbook of Metrology and Applications* (Springer, 2022) pp. 1–23.

[20] T. Fortier and E. Baumann, Commun. Phys. **2**, 153 (2019).

[21] G. K. Campbell and W. D. Phillips, Phil. Trans. R. Soc. A. **369**, 4078 (2011).

[22] P. Gill, J. Phys. Conf. Ser. **723**, 012053 (2016).

[23] A. Sørensen and K. Mølmer, Phys. Rev. Lett. **83**, 2274 (1999).

[24] J. J. Bollinger, W. M. Itano, D. J. Wineland, and D. J. Heinzen, Phys. Rev. A. **54**, R4649 (1996).

[25] S. F. Huelga, C. Macchiavello, T. Pellizzari, A. K. Ekert, M. B. Plenio, and J. I. Cirac, Phys. Rev. Lett. **79**, 3865 (1997).

[26] B. Escher, R. de Matos Filho, and L. Davidovich, Nat. Phys.. **7**, 406 (2011).

[27] R. Demkowicz-Dobrzański, J. Kołodyński, and M. Guţă, Nat. Commun. **3**, 1 (2012).

[28] A. W. Chin, S. F. Huelga, and M. B. Plenio, Phys. Rev. Lett. **109**, 233601 (2012).

[29] R. Chaves, J. B. Brask, M. Markiewicz, J. Kołodyński, and A. Acín, Phys. Rev. Lett. **111**, 120401 (2013).

[30] J. B. Brask, R. Chaves, and J. Kołodyński, Phys. Rev. X. **5**, 031010 (2015).

[31] I. D. Leroux, M. H. Schleier-Smith, and V. Vuletić, Phys. Rev. Lett. **104**, 250801 (2010).

[32] A. Louchet-Chauvet, J. Appel, J. J. Renema, D. Oblak, N. Kjaergaard, and E. S. Polzik, New J. Phys. **12**, 065032 (2010).

[33] O. Hosten, N. J. Engelsen, R. Krishnakumar, and M. A. Kasevich, Nature **529**, 505 (2016).

[34] S. Zhou, M. Zhang, J. Preskill, and L. Jiang, Nat. Commun. **9**, 1 (2018).

[35] P. Sekatski, M. Skotiniotis, J. Kołodyński, and W. Dür, Quantum **1**, 27 (2017).

[36] R. Demkowicz-Dobrzański, J. Czajkowski, and P. Sekatski, Phys. Rev. X **7**, 041009 (2017).

[37] M. Xu and M. J. Holland, Phys. Rev. Lett. **114**, 103601 (2015).

[38] H. Smith, Proc. IEEE **60**, 479 (1972).

[39] J. A. Barnes, Time and Frequency: Theory and Fundamentals **140**, 1 (1974).

[40] P. K. Seidelmann and J. H. Seago, Metrologia **48**, S186 (2011).

[41] D. D. McCarthy, Metrologia **48**, S132 (2011).

[42] E. F. Arias, Phil. Trans. R. Soc. A. **363**, 2289 (2005).

[43] H. Chadsey and D. McCarthy, in *PTTI* (2000) pp. 237–254.

[44] B. Guinot, Metrologia **31**, 431 (1995).

[45] G. Panfilo, IEEE Instrum. Meas. Mag. **19**, 28 (2016).

[46] P. Tavella and C. Thomas, Metrologia **28**, 57 (1991).

[47] "BIPM Circular T," (2023).

[48] T. Quinn, Proc. IEEE **79**, 894 (1991).

[49] P. B. Whibberley, J. A. Davis, and S. L. Shemar, Metrologia **48**, S154 (2011).

[50] J. Levine and T. Parker, in *IFCS + PDA (Cat. No.02CH37234)* (2002) pp. 537–542.

[51] I. Sesia, G. Signorile, T. T. Thai, P. Defraigne, and P. Tavella, GPS Solut. **25**, 61 (2021).

[52] D. J. Berkeland, J. D. Miller, J. C. Bergquist, W. M. Itano, and D. J. Wineland, Phys. Rev. Lett. **80**, 2089 (1998).

[53] S. R. Jefferts, T. P. Heavner, and E. A. Donley, Japanese J. Appl. Phys. **43**, 2803 (2004).

[54] A. Bauch, MITTEILUNGEN S , 25 (2012).

[55] D. D. McCarthy, Proc. Int. Astron. Union **2004**, 180–197 (2004).

[56] G. Panfilo, A. Harmegnies, and L. Tisserand, Metrologia **49**, 49 (2011).

[57] G. Panfilo, A. Harmegnies, and L. Tisserand, Metrologia **51**, 285 (2014).

[58] G. rard Petit, Metrologia **40**, S252 (2003).

[59] J. Azoubib, M. Granveaud, and B. Guinot, Metrologia **13**, 87 (1977).

[60] G. Panfilo and E. F. Arias, IEEE Trans. Ultrason. Ferroelectr. Freq. Control. **57**, 154 (2010).

[61] D. Allan and M. Weiss, in *34th Annual Symposium on Frequency Control* (1980) pp. 334–346.

[62] G. Petit and Z. Jiang, Metrologia **45**, 35 (2007).

[63] G. Petit and Z. Jiang, Int. J. Navig. Obs. **2008**, 562878 (2008).

[64] *Annual Report of the BIPM Time Section*, Tech. Rep. (2020).

[65] D. Hanson, in *Proceedings of the 43rd Annual Symposium on Frequency Control* (1989) pp. 174–178.

[66] L. Galleani, Metrologia **45**, S175 (2008).

[67] J. Rutman, Proc. IEEE **66**, 1048 (1978).

[68] L. Galleani and P. Tavella, IEEE Control Syst. Mag. **30**, 44 (2010).

[69] P. Tavella, Metrologia **45**, S183 (2008).

[70] W. J. Riley, *Handbook of Frequency* (NIST, Boulder, 2008).

[71] J. Levine, Rev. Sci. Instrum. **70**, 2567 (1999).

[72] J. Rutman and F. Walls, Proc. IEEE **79**, 952 (1991).

[73] S. R. Stein, in *Frequency and Time, Their Measurement and Characterization, Precision Frequency Controls*, Vol. 2 (Academic, New York, 1985) Chap. 12.

[74] D. B. Sullivan, D. W. Allan, D. A. Howe, D. Sullivan, and F. Walls, *Characterization of clocks and oscillators* (US Department of Commerce, National Institute of Standards and Technology, 1990).

[75] E. Ferre-Pikal, J. Vig, J. Camparo, L. Cutler, L. Maleki, W. Riley, S. Stein, C. Thomas, F. Walls, and J. White, in *Proc. IFCS* (1997) pp. 338–357.

[76] G. Panfilo and P. Tavella, Metrologia **45**, S108 (2008).

[77] E. Nunzi, G. Panfilo, P. Tavella, P. Carbone, and D. Petri, IEEE Trans. Instrum. Meas. **54**, 1565 (2005).

[78] L. Galleani, L. Sacerdote, P. Tavella, and C. Zucca, Metrologia **40**, S257 (2003).

[79] E. Bibbona, G. Panfilo, and P. Tavella, Metrologia **45**, S117 (2008).

[80] C. Zucca and P. Tavella, IEEE Trans. Ultrason. Ferroelectr. Freq. Control. **52**, 289 (2005).

[81] J. Chaffee, IEEE Trans. Ultrason. Ferroelectr. Freq. Control **34**, 655 (1987).

[82] N. F. Ramsey, Phys. Rev. **78**, 695 (1950).

[83] N. F. Ramsey, Rev. Mod. Phys. **62**, 541 (1990).

[84] L. M. K. Vandersypen and I. L. Chuang, Rev. Mod. Phys. **76**, 1037 (2005).

[85] M. A. Nielsen and I. L. Chuang, *Quantum computation and Quantum information* (Cambridge University Press, Cambridge, England, 2000).

[86] W. M. Itano, J. C. Bergquist, J. J. Bollinger, J. M. Gilligan, D. J. Heinzen, F. L. Moore, M. G. Raizen, and D. J. Wineland, Phys. Rev. A. **47**, 3554 (1993).

[87] H. Ku, J. Res. National Bureau Standards **70C**, 263 (1966).

[88] S. L. Campbell, R. B. Hutson, G. E. Marti, A. Goban, N. D. Oppong, R. L. McNally, L. Sonderhouse, J. M. Robinson, W. Zhang, B. J. Bloom, and J. Ye, Science **358**, 90 (2017).

[89] F. Levi, D. Calonico, L. Lorini, and A. Godone, Metrologia **43**, 545 (2006).

[90] W. M. Itano, J. C. Bergquist, J. J. Bollinger, J. M. Gilligan, D. J. Heinzen, F. L. Moore, M. G. Raizen, and D. J. Wineland, Phys. Rev. A. **47**, 3554 (1993).

[91] P. Kómár, E. M. Kessler, M. Bishof, L. Jiang, A. S. Sørensen, J. Ye, and M. D. Lukin, Nat. Phys. **10**, 582 (2014).

[92] D. J. Wineland, C. Monroe, W. M. Itano, D. Leibfried, B. E. King, and D. M. Meekhof, J. Res. Natl. Inst. Stand. Technol. **103**, 259 (1998).

[93] S. Huelga, P. Knight, C. Macchiavello, M. Plenio, and V. Vedral, Appl. Phys. B **67**, 723 (1998).

[94] C. C. Gerry and P. L. Knight, in *Introductory Quantum Optics* (Cambridge University Press, Cambridge, 2005) Chap. 7, pp. 150–194.

[95] K. P. Seshadreesan, J. P. Dowling, and G. S. Agarwal, Physica Scripta **90**, 074029 (2015).

[96] D. J. Griffiths and D. F. Schroeter, *Introduction to Quantum Mechanics*, 3rd ed. (Cambridge University Press, Cambridge, 2018).

[97] N. Govindarajan, R. Mohr, S. Chandrasekaran, and I. Mezic, SIAM Journal on Applied Dynamical Systems **18**, 1454 (2019).

[98] B. Øksendal, "Itô integrals," in *Stochastic Differential Equations: An Introduction with Applications* (Springer Berlin Heidelberg, Berlin, Heidelberg, 2003) pp. 21–42.

[99] G. Panfilo, G. Petit, and A. Harmegnies, Metrologia **57**, 065011 (2020).

[100] P. Tavella and C. Thomas, Metrologia **28**, 57 (1991).

[101] C. Thomas and J. Azoubib, Metrologia **33**, 227 (1996).

[102] C. Thomas and J. Azoubib, in *PTTI* (1997) pp. 7–18.

[103] J. Azoubib, in *PTTI* (2000) pp. 195–210.

[104] *Annual Report of the BIPM Time Section*, Tech. Rep. (1998).

Appendix A

ALGOS prediction algorithm

Here I provide more details about the ALGOS algorithm. I start with proving Eq. (3.3). We notice that

$$\sum_{i=1}^{N} w_i = 1. \tag{A.1}$$

Using Eq. (A.1) and Eq. (3.1), we have

$$\sum_{i=1}^{N} w_i \left[\mathrm{EAL}(t) - h_i(t)\right] = \sum_{i=1}^{N} w_i h_i'(t). \tag{A.2}$$

We add and subtract $h_j(t)$ from the left hand side of Eq. (A.2):

$$\sum_{i=1}^{N} w_i \left[\mathrm{EAL}(t) - h_i(t) + h_j(t) - h_j(t)\right] = \sum_{i=1}^{N} w_i h_i'(t). \tag{A.3}$$

Using Eq. (3.2), we have

$$\sum_{i=1}^{N} w_i \left[\mathrm{EAL}(t) - h_j(t) + x_{i,j}(t)\right] = \sum_{i=1}^{N} w_i h_i'(t). \tag{A.4}$$

Finally, we have

$$\mathrm{EAL}(t) - h_j(t) = \sum_{i=1}^{N} w_i \left[h_i'(t) - x_{i,j}(t)\right]. \tag{A.5}$$

Now we present a rigorous proof of Eq. (3.4) by sequentially proving Eqs (3.5) and (3.6). Subsequently, we elucidate the integration of the frequency drift term, C_{i,I_k}, into Eq. (3.4).

A.1 Time continuity of EAL

To prove Eq. (3.5), we commence with

$$\begin{aligned} \mathrm{EAL}_{I_{k-1}}(t) &= \sum_{i=1}^{N_{I_{k-1}}} w_{i,I_{k-1}} h_i(t) \\ \mathrm{EAL}_{I_k}(t) &= \sum_{i=1}^{N_{I_k}} w_{i,I_k} h_i(t). \end{aligned} \tag{A.6}$$

We intentionally exclude $h_i'(t)$ as our objective is to derive it. The terms $\mathrm{EAL}_{I_{k-1}}(t)$ and $\mathrm{EAL}_{I_k}(t)$ signify the computation of EAL in the intervals I_{k-1} and I_k, respectively. We introduce subscripts to account for the variation in the number of clocks and weights during each EAL calculation interval.

To maintain time continuity, we incorporate a correction term, A, to $\mathrm{EAL}_{I_k}(t)$

$$\mathrm{EAL}_{I_k}(t) = \sum_{i=1}^{N_{I_k}} [w_{i,I_k} h_i(t)] + A. \tag{A.7}$$

We need

$$\mathrm{EAL}_{I_{k-1}}(t_k) = \mathrm{EAL}_{I_k}(t_k). \tag{A.8}$$

Consequently,

$$A = \mathrm{EAL}_{I_{k-1}}(t_k) - \sum_{i=1}^{N_{I_k}} w_{i,I_k} h_i(t_k). \tag{A.9}$$

Using Eq. (A.1), we obtain

$$A = \sum_{i=1}^{N_{I_k}} w_{i,I_k} \left[\mathrm{EAL}_{I_{k-1}}(t_k) - h_i(t_k)\right]. \tag{A.10}$$

Defining

$$x_{i,I_{k-1}}(t_k) := \mathrm{EAL}_{I_{k-1}}(t_k) - h_i(t_k) \tag{A.11}$$

as outlined in Eq. (3.5), complete our derivation of the first term in Eq. (3.4).

A.2 Frequency continuity of EAL

To ensure frequency continuity, we incorporate an additional correction term into $\mathrm{EAL}_{I_k}(t)$

$$\mathrm{EAL}_{I_k}(t) = \sum_{i=1}^{N_{I_k}} [w_{i,I_k} h_i(t)] + A + B(t - t_k). \tag{A.12}$$

To derive B, we first introduce the following notations:

$$\begin{aligned} f_{\mathrm{EAL}_{I_{k-1}}}(t) &:= \frac{\mathrm{dEAL}_{I_{k-1}}(t)}{\mathrm{d}t} \\ f_{\mathrm{EAL}_{I_k}}(t) &:= \frac{\mathrm{dEAL}_{I_k}(t)}{\mathrm{d}t} \\ f_{h_i}(t) &:= \frac{\mathrm{d}h_i(t)}{\mathrm{d}t}, \end{aligned} \tag{A.13}$$

where $f_{\mathrm{EAL}_{Ik-1}}(t)$ and $f_{\mathrm{EAL}_{Ik}}(t)$ represent the EAL frequency in intervals I_{k-1} and I_k, respectively, and $f_{h_i}(t)$ denotes the frequency of clock H_i. We proceed with

$$\begin{aligned} f_{\mathrm{EAL}_{I_{k-1}}}(t_k) &= \sum_{i=1}^{N_{I_{k-1}}} w_{i,I_{k-1}} f_{h_i}(t_k) \\ f_{\mathrm{EAL}_{I_k}}(t_k) &= \sum_{i=1}^{N_{I_k}} [w_{i,I_k} f_{h_i}(t_k)] + B. \end{aligned} \tag{A.14}$$

We need

$$f_{\mathrm{EAL}_{I_{k-1}}}(t_k) = f_{\mathrm{EAL}_{I_k}}(t_k). \tag{A.15}$$

From Eq. (A.14), we deduce

$$B = f_{\mathrm{EAL}_{I_{k-1}}}(t_k) - \sum_{i=1}^{N_{I_k}} w_{i,I_k} f_{h_i}(t_k). \tag{A.16}$$

However, instantaneous frequencies at t_k are unavailable. We assume that the frequency of EAL is constant during its calculation interval. Thus,

$$\begin{aligned} \mathrm{EAL}_{I_{k-1}}(t_k) &= \mathrm{EAL}_{I_{k-1}}(t_{k-1}) + f_{\mathrm{EAL}_{I_{k-1}}} \times (t_k - t_{k-1}) \\ h_i(t_{k+1}) &= h_i(t_k) + f_{h_i} \times (t_{k+1} - t_k). \end{aligned} \tag{A.17}$$

By solving for $f_{\mathrm{EAL}_{I_{k-1}}}$ and f_{h_i} in Eq. (A.17) and substituting into Eq. (A.16), we obtain

$$B = \frac{\mathrm{EAL}_{I_{k-1}}(t_k) - \mathrm{EAL}_{I_{k-1}}(t_{k-1})}{t_k - t_{k-1}} - \sum_{i=1}^{N_k} w_{i,I_k} \frac{h_i(t_{k+1}) - h_i(t_k)}{t_{k+1} - t_k}. \tag{A.18}$$

Using Eq. (A.1), we derive

$$B = \sum_{i=1}^{N_k} w_{i,I_k} \left[\frac{\mathrm{EAL}_{I_{k-1}}(t_k) - \mathrm{EAL}_{I_{k-1}}(t_{k-1})}{t_k - t_{k-1}} - \frac{h_i(t_{k+1}) - h_i(t_k)}{t_{k+1} - t_k} \right]. \tag{A.19}$$

We assume the frequency of clocks is equal during each interval, i.e.,

$$\frac{h_i(t_{k+1}) - h_i(t_k)}{t_{k+1} - t_k} = \frac{h_i(t_k) - h_i(t_{k-1})}{t_k - t_{k-1}}. \tag{A.20}$$

Substituting Eq. (A.20) into Eq. (A.19), we arrive at

$$B = \sum_{i=1}^{N_k} w_{i,I_k} \left[\frac{\mathrm{EAL}_{I_{k-1}}(t_k) - h_i(t_k) - \mathrm{EAL}_{I_{k-1}}(t_{k-1}) + h_i(t_{k-1})}{t_k - t_{k-1}} \right]. \tag{A.21}$$

Utilizing Eq. (A.11), we deduce

$$B = \sum_{i=1}^{N_k} w_{i,I_k} \frac{x_{i,I_{k-1}}(t_k) - x_{i,I_{k-1}}(t_{k-1})}{t_k - t_{k-1}}. \tag{A.22}$$

Defining

$$y_{i,I_{k-1}} := \frac{x_{i,I_{k-1}}(t_k) - x_{i,I_{k-1}}(t_{k-1})}{t_k - t_{k-1}} \tag{A.23}$$

as outlined in Eq. (3.6), complete our derivation of the second term in Eq. (3.4).

A.3 Frequency drift

To ensure the continuity of the frequency drift in the EAL, we introduce an additional correction term to $\mathrm{EAL}_{I_k}(t)$ as follows

$$\mathrm{EAL}_{I_k}(t) = \sum_{i=1}^{N_{I_k}} [w_{i,I_k} h_i(t)] + A + B(t - t_k) + \frac{1}{2}C(t - t_k)^2, \tag{A.24}$$

where

$$C = \sum_{i=1}^{N_{I_k}} C_{i,I_k}, \tag{A.25}$$

and C_{i,I_k} is the frequency drift of each clock with respect to EAL in the I_k interval. We subsequently rewrite Eq. (A.17) to include the frequency drift as

$$\begin{aligned} \mathrm{EAL}_{I_{k-1}}(t_k) &= \mathrm{EAL}_{I_{k-1}}(t_{k-1}) + f_{\mathrm{EAL}_{I_{k-1}}}(t_{k-1}) \times (t_k - t_{k-1}) + \frac{1}{2} f'_{I_{k-1}} \times (t_k - t_{k-1})^2 \\ h_i(t_{k+1}) &= h_i(t_k) + f_{h_i}(t_k) \times (t_{k+1} - t_k) + \frac{1}{2} \times f'_{i,I_k}(t_{k+1} - t_k)^2, \end{aligned} \tag{A.26}$$

with f' representing the frequency drift, assumed to be constant. Consequently,

$$\begin{aligned} \frac{\mathrm{EAL}_{I_{k-1}}(t_k) - \mathrm{EAL}_{I_{k-1}}(t_{k-1})}{t_k - t_{k-1}} &= f_{\mathrm{EAL}_{I_{k-1}}}(t_{k-1}) + \frac{1}{2} f'_{I_{k-1}} \times (t_k - t_{k-1}) \\ \frac{h_i(t_{k+1}) - h_i(t_k)}{t_{k+1} - t_k} &= f_{h_i}(t_k) + \frac{1}{2} f'_{i,I_k} \times (t_{k+1} - t_k). \end{aligned} \tag{A.27}$$

We also have

$$f_{\mathrm{EAL}_{I_{k-1}}}(t_k) = f_{\mathrm{EAL}_{I_{k-1}}}(t_{k-1}) + f'_{I_{k-1}} \times (t_k - t_{k-1}). \tag{A.28}$$

As a result, we have

$$\begin{aligned} f_{\mathrm{EAL}_{I_{k-1}}}(t_k) &= \frac{\mathrm{EAL}_{I_{k-1}}(t_k) - \mathrm{EAL}_{I_{k-1}}(t_{k-1})}{t_k - t_{k-1}} + \frac{1}{2} f'_{I_{k-1}} \times (t_k - t_{k-1}) \\ f_{h_i}(t_k) &= \frac{h_i(t_{k+1}) - h_i(t_k)}{t_{k+1} - t_k} - \frac{1}{2} f'_{i,I_k}(t_{k+1} - t_k) \end{aligned} \tag{A.29}$$

By substituting $f_{\mathrm{EAL}_{I_{k-1}}}(t_k)$ and $f_{h_i}(t_k)$ into Eq. (A.16), we obtain

$$\begin{aligned} B = \sum_{i=1}^{N_k} w_{i,I_k} \Bigg[&\frac{\mathrm{EAL}_{I_{k-1}}(t_k) - \mathrm{EAL}_{I_{k-1}}(t_{k-1})}{t_k - t_{k-1}} - \frac{h_i(t_{k+1}) - h_i(t_k)}{t_{k+1} - t_k} \\ &+ \frac{1}{2} f'_{I_{k-1}}(t_k - t_{k-1}) + \frac{1}{2} f'_{i,I_k}(t_{k+1} - t_k) \Bigg]. \end{aligned} \tag{A.30}$$

We note that

$$\begin{aligned} h_i(t_{k+1}) &= h_i(t_k) + f_{h_i}(t_k)(t_{k+1} - t_k) + \frac{1}{2} f'_{i,I_k} \times (t_{k+1} - t_k)^2 \\ h_i(t_k) &= h_i(t_{k-1}) + f_{h_i}(t_{k-1})(t_k - t_{k-1}) + \frac{1}{2} f'_{i,I_{k-1}} \times (t_k - t_{k-1})^2. \end{aligned} \tag{A.31}$$

Therefore,

$$f_{h_i}(t_k) = \frac{h_i(t_{k+1}) - h_i(t_k)}{t_{k+1} - t_k} - \frac{1}{2} f'_{i,I_k} \times (t_{k+1} - t_k) \tag{A.32}$$

$$f_{h_i}(t_{k-1}) = \frac{h_i(t_k) - h_i(t_{k-1})}{t_k - t_{k-1}} - \frac{1}{2} f'_{i,I_{k-1}} \times (t_k - t_{k-1}). \tag{A.33}$$

On the other hand, we have

$$f_{h_i}(t_k) = f_{h_i}(t_{k-1}) + f'_{i,I_{k-1}} \times (t_k - t_{k-1}). \tag{A.34}$$

By solving for $f'_{i,I_{k-1}}$ in Eq. (A.34) and substituting into Eq. (A.33), we derive

$$f_{h_i}(t_k) = \frac{h_i(t_k) - h_i(t_{k-1})}{t_k - t_{k-1}} + \frac{1}{2} f'_{i,I_{k-1}} \times (t_k - t_{k-1}). \tag{A.35}$$

Equation (A.32) and Eq. (A.35) are equal. Thus,

$$\frac{h_i(t_{k+1}) - h_i(t_k)}{t_{k+1} - t_k} = \frac{h_i(t_k) - h_i(t_{k-1})}{t_k - t_{k-1}} + \frac{1}{2} f'_{i,I_k} \times (t_{k+1} - t_k) + \frac{1}{2} f'_{i,I_{k-1}} \times (t_k - t_{k-1}). \quad \text{(A.36)}$$

We assume $f'_{i,I_k} = f'_{i,I_{k-1}}$ and $t_{k+1} - t_k = t_k - t_{k-1}$. Consequently,

$$\frac{h_i(t_{k+1}) - h_i(t_k)}{t_{k+1} - t_k} = \frac{h_i(t_k) - h_i(t_{k-1})}{t_k - t_{k-1}} + f'_{i,I_k} \times (t_k - t_{k-1}) \quad \text{(A.37)}$$

By substituting Eq. (A.37) into Eq. (A.30) and using $t_{k+1} - t_k = t_k - t_{k-1}$, we deduce

$$B = \sum_{i=1}^{N_k} w_{i,I_k} \left[\frac{x_i(t_k) - x_i(t_{k-1})}{t_k - t_{k-1}} + \frac{1}{2} \left(f'_{I_{k-1}} - f'_{i,I_k} \right) (t_k - t_{k-1}) \right]. \quad \text{(A.38)}$$

By using Eq. (A.23) and Eq. (A.25), we obtain

$$B = \sum_{i=1}^{N_k} w_{i,I_k} \left[y_{i,I_{k-1}} + \frac{1}{2} C_{i,I_{k-1}} (t_k - t_{k-1}) \right]. \quad \text{(A.39)}$$

Finally, we have obtained all the correction terms. By substituting Eq. (A.10), Eq. (A.39), and Eq. (A.25) into Eq. (A.24), we derive

$$\begin{aligned} \mathrm{EAL}_{I_k}(t) = \sum_{i=1}^{N_{I_k}} w_{i,I_k} \Big[& h_i(t) + x_i(t_k) + y_{i,I_{k-1}}(t - t_k) + \frac{1}{2} C_{i,I_{k-1}} (t_k - t_{k-1})(t - t_k) \\ & + \frac{1}{2} C_{i,I_k} (t - t_k)^2 \Big]. \end{aligned} \quad \text{(A.40)}$$

Assuming $C_{i,I_{k-1}} = C_{i,I_k}$, we define

$$h'_{i,I_k}(t) := x_{i,I_{k-1}}(t_k) + y_{i,I_{k-1}}(t - t_k) + \frac{1}{2} C_{i,I_k} (t_k - t_{k-1})(t - t_k) + \frac{1}{2} C_{i,I_k} (t - t_k)^2, \quad \text{(A.41)}$$

as outined in Eq. (3.4). By substituting Eq. (A.41) into Eq. (A.40), we obtain

$$\mathrm{EAL}_{I_k}(t) = \sum_{i=1}^{N_{I_k}} w_{i,I_k} \left[h_i(t) + h'_{i,I_k}(t) \right]. \tag{A.42}$$

as outlined in Eq. (3.1).

Appendix B

Weighting algorithm

In this appendix, we elucidate the progression of weighting algorithms. Initially, we present the approach employed prior to January 1, 1998, as detailed in [100]. Subsequently, we expound upon the technique utilized until January 2001, drawing from [101, 102, 103]. As of January 1, 2014, the weighting algorithm delineated in §3.2 has been adopted. The rationale underpinning the current methodology's implementation is thoroughly examined in §B.3.

B.1 Weighting algorithm until January 1, 1998

The clock weights were ascertained through a four-iteration process, executed as follows [100]:

(1) Employing a specified set of absolute weights, the values $x_{i,I_k}(t)$ are derived. In the initial iteration, the weights stem from the preceding computation interval, while subsequent iterations utilize weights from the prior iteration.

(2) Utilizing the $x_{i,I_k}(t)$ values, frequency deviations y_{i,I_k} are determined for each clock.

(3) Individual variances $\sigma_i^2(6,T)$ are calculated for y_{i,I_k} along with the preceding five two-month frequency deviations. Here, the variable T represents the calculation interval's duration, which spanned two months until 1 Jan 1998.

(4) A temporary value p_i' is employed to compute the weight of clock H_i according to the following equation:

$$p_i' = \frac{10000}{\sigma_i^2(6,T)}, \tag{B.1}$$

where the factor 10000 is selected arbitrarily.

(5) The updated weight p_i is equal to p_i', except for two specific scenarios:

(a) If $\sigma_i^2(6,T) < 3.16\,{}^{\text{ns}}/_{\text{day}}$, then $p_i = 1000$.

(b) If clock H_i exhibits abnormal behaviour, then $p_i = 0$.

By imposing a lower limit on $\sigma_i^2(6,T)$ in part **(a)**, an upper boundary is set for p_i. This constraint is essential for preventing a limited number of superior clocks from dominating the time scale, ensuring its reliability. However, this restriction also implies that the time scale's stability may not surpass that of the best clocks within the network.

To identify abnormal behaviour as described in part **(b)**, the average $\bar{y}_i$ and the variance $s_i^2(5,T)$ of the frequency deviations across the last five two-month intervals are initially computed for each clock. Assuming random walk frequency noise, a six-sample variance $s_i^2(6,T)$ is subsequently estimated using $s_i^2(6,T) = ({}^6/_5)\, s_i^2(5,T)$. With the condition

$$\text{if } s_i^2(6,T) \le \sigma_{\min}^2 = 3.16\,{}^{\text{ns}}/_{\text{day}}, \text{ then } s_i^2(6,T) = \sigma_{\min}^2, \tag{B.2}$$

Abnormal behaviour is detected when

$$\frac{y_{i,I_k} - \bar{y}_i}{s_i(6,T)} \ge 3. \tag{B.3}$$

B.2 Weighting algorithm until January 1, 2014

An alternative method for constraining individual clock contributions involves selecting a maximum relative weight $w_{\max}$ rather than an absolute weight $p_{\max}$. This strategy is em-

ployed since January 1, 1998. Another modification implemented on January 1, 1998, involved changing the EAL calculation interval T from two months to one month.

Steps **(1)** and **(2)** remained unchanged in the updated algorithm. In step **(3)**, the new algorithm utilized $\sigma^2(12, T)$ with $T = 30$ days, as opposed to $\sigma^2(6, T)$ with $T = 60$ days. Steps four and five were redefined as follows:

(4) The relative weight of clock H_i is determined using a temporary value as expressed in

$$w_{i,\text{temp}} = \frac{1/\sigma_i^2(12,T)}{\sum_{i=1}^{N} 1/\sigma_i^2(12,T)}. \tag{B.4}$$

(5) The updated weight w_i is equal to $w_{i,\text{temp}}$, barring two exceptions:

(a) If $w_i > w_{\max}$, then $w_i = w_{\max}$.

(b) If clock H_i exhibits abnormal behaviour, then $w_i = 0$.

However, implementing exceptions **(a)** and **(b)** presents challenges. First, individual relative weights are either forced to be equal to $w_{\max}$ or zero, causing the sum of relative weights to deviate from 1. Second, no value for $\sigma_{\min}$ is specified to define the maximum permitted stability when applying the criterion for detecting abnormal behaviour. Addressing these issues requires a two sets of sub-iteration process within each iteration of the general computational procedure described earlier.

The first set of sub-iteration commences with the temporary weights computed in Eq.(B.4). Upon applying condition **(a)** and normalizing the temporary weights, multiple sub-iterations are necessary because each normalization increases the temporary weight of clocks that have not yet reached $w_{\max}$, potentially necessitating additional normalization. This first set of sub-iterations concludes when no additional clocks reach $w_{\max}$ following normalization.

Subsequently, the last clock to attain $w_{\max}$ is identified as the least stable among those achieving $w_{\max}$. The frequency variance of this clock, $\sigma_i^2(12, T)$, serves as $\sigma_{\min}^2$. Abnormal

behavior can thus be detected as before. However, after identifying abnormal behavior, some clocks receive a weight of zero, necessitating a second set of sub-iteration sequence to normalize the weights once more. Ultimately, a normalized weight set is obtained in which both conditions **(a)** and **(b)** are satisfied.

Initially, the maximum relative weight was set at 0.7%, corresponding to $p_{\max} = 2500$ in November/December 1997 [104]. However, in 2000, it was realized that 0.7% was insufficient for differentiating the best-performing clocks. Consequently, $w_{\max}$ was set as A/N, where A represents an empirical constant and N denotes the number of clocks. In 2000, it was determined that the optimal value for A was 2.5, as it would ensure both EAL reliability and enhanced stability. Nevertheless, this abrupt change threatened EAL continuity. As a result, it was proposed to utilize $A = 2$ from January 2001 to December 2001 and then transition to $A = 2.5$ from January 2002 onwards [103].

B.3 Weighting algorithm since January 1, 2014

In 2011, a modification to the prediction algorithm substantially enhanced the stability of UTC by accounting for the frequency drift of clocks [56]. However, the weighting process remained unchanged, as it was a distinct procedure.

The weighting algorithm takes into account the values of $\sigma_i^2(12, T)$. Lower values correspond to higher weights, thus allocating greater weights to more stable clocks while reducing the weights of clocks affected by frequency drift. In 2014, a novel weighting algorithm was proposed [57], shifting focus from $\sigma_i^2(12, T)$ to the predictability of a clock's performance. As a result, even clocks with frequency drift could obtain high weights if their behaviour was predictable.

This new weighting algorithm evaluates the predicted performance against the actual performance of atomic clocks, determining their weights based on this comparison. Prior to 2014, a low $\sigma_i^2(12, T)$ value defined a good clock; however, with the new algorithm, a

"good clock is a predictable clock" [57]. For reference, Tab. B.1 illustrates the evolution of maximum weights.

Date	Maximum weight
Until 1 Jan 1988	$p_{\max} = 200$
Until 2 May 1995	$p_{\max} = 1000$
Until 1 Jan 1998	$p_{\max} = 2500$
Until 1 Jan 2001	$w_{\max} = 0.7\%$
Until 1 Jan 2002	$w_{\max} = {}^{2}/_{N}$
Until 1 Jan 2014	$w_{\max} = {}^{2.5}/_{N}$
Since 1 Jan 2014	$w_{\max} = {}^{4}/_{N}$

Table B.1: The evolution of the maximum weight.